RESEARCH ARTICLE

WILEY

An enriched mixed finite element model for the simulation of microseismic and acoustic emissions in fractured porous media with multi-phase flow and thermal coupling

Mohammad Komijani[1,2] 🆔 | **Peter Wriggers[1]** | **Taha Goudarzi[2]**

[1]Institute of Continuum Mechanics, Leibniz University Hannover, Honnover, Germany

[2]Department of Mechanical Engineering, Amirkabir University of Technology, Tehran, Iran

Correspondence
Mohammad Komijani, Department of Mechanical Engineering, Amirkabir University of Technology, Tehran, Iran.
Email: m.komijani@aut.ac.ir

Abstract

A novel mixed enriched finite element model is developed for coupled non-linear thermo-hydro-mechanical simulation of fractured porous media with three-phase flow and thermal coupling. Simulation of induced acoustic emission (AE) and microseismic emission (ME) due to tensile fracturing and shear slip instability of pre-existing fracture interfaces is carried out and the numerical results of the emitted signals are analysed. The mathematical model is based on the generalized Biot's theory for coupled interaction of solid and fluid phases. A computationally robust non-linear solver is developed to handle the severe non-linearities arising from fluid saturations, relative permeabilities of fluids, constitutive models of interfaces and convective thermal coupling. To model pre-existing natural fractures and faults, discrete fracture propagation and nucleation of cracks (micro-cracking) independently of the original mesh topology, a local Partition-of-Unity (PU) finite element method, namely, the Phantom Node Method (PNM) is implemented. The cohesive fracture modelling scheme is implemented to account for the non-linear behaviour of fracturing and localization, and to rectify the non-physical stress singularity condition at the fracture tip. Effects of different system parameters on fracturing, shear-slip instability and the associated induced AEs and MEs are investigated through various numerical results.

KEYWORDS
acoustic emission, microseismic emission, multi-phase flow, porous media, thermo-hydro-mechanical coupling

1 | INTRODUCTION

A porous medium is comprised of a solid skeleton with pore spaces that are filled with one or more fluid phases. The multi-physics behaviour of the mixture is governed by the interaction of the solid and fluid constituents. Porous media analysis has a vast variety of applications from reservoir geomechanics[1] to biomechanics of tissues and cells.[2,3] A significant amount of effort has been dedicated to modelling of saturated and partially saturated porous media. In porous media analysis, it is assumed that the pore spaces are filled by a single- or multi-phase fluid. In multi-phase porous media, the pore spaces are filled with more than one fluid phase and the concept of volume fractions is used to determine the

portion of each fluid phase in the mixture. Saturation of each phase is defined as the ratio of the volume of that phase to the total pore volume in a representative elementary volume (REV). The saturation variables are denoted as experimentally determined functions of the capillary pressures (i.e. the difference between the non-wetting fluid phase pressure and the wetting fluid phase pressure). The interaction between fluid phases is accommodated through the concept of relative permeabilities which are specified as empirical functions of fluid saturations.

Porous media analysis with multi-phase flow has a wide scope of applications in sub-surface engineering for geo-containment and hydrocarbon extractions. Simulation of groundwater contamination by industrial chemicals and hydrocarbons in applications like waste injection, modelling of steam and water injection in reservoir stimulation processes for enhanced recovery, and seismic and slope stability analysis in porous formations are only a few to be noted. Several papers have been published recently on the topic of fractured and non-fractured porous media with single- and multi-phase fluid flow with potential application in geomechanics.[4–9]

Several numerical models have been proposed over decades for simulation of porous media with multi-phase flow. Depending on the focus of the projects and objectives, the reported works have limitations and restrictions. Many of the reported works deal with the modelling of fluid flows while neglecting the interaction of fluids with deformable solid.[10–12] In most of the developed models, the transient (but not dynamic) behaviour of the fluid phase is considered, whereas the solid skeleton is assumed to deform in a quasi-static manner. Taking the inertia/dynamic effects into account becomes prominent when simulation of porous media under dynamic (moderate to high-frequency) loadings is of interest. Also, simulation of dynamic fracture propagation and induced acoustic/seismic emission requires inclusion of the inertia terms. Recently, Cao et al.[13] simulated the stepwise process of fracturing in porous media and the associated fluid pressure oscillations using the standard FEM and Rethore et al.[14] modelled the dynamic propagation of shear bands in saturated porous media. Despite considering the inertia effects, simulation of wave propagation and induced acoustic emission (AE) in porous media with multi-phase flow and thermal coupling has not been the focus of the earlier works.

AEs and microseismic emissions (ME) which appear in the form of high-frequency mechanical wave propagations are the results of abrupt release of stored strain energy in a rock matrix[15] due to tensile (AE) and shear (ME) type material failures. In naturally fractured geological formations, induced wave emissions are generated by rapid stress degradation and localizations such as pre-existing fracture/fault reactivation in the form of shear-slip instability, crack extension and micro-cracking/nucleation. AE and ME monitoring has been extensively used in vast variety of practical engineering application such as, damage and health monitoring in concrete and masonry structures,[16–18] and rock mass deformation and cracking/damaging in mining and hydraulic fracturing (HF) applications.[19,20] As an example, AE and ME monitoring is a widely used technique for evaluation of the extent and trajectory of the induced cracks, and to notice reactivation of natural faults/fractures in sub-surface hydraulic stimulation processes.[21]

The focus of the most of the research works previously reported on modelling-induced AE has been on developing correlations between the energy released due to fracturing and the acoustic event magnitude and moment, without any explicit incorporation of the coupled behaviour of localization and the associated induced AE in the form of mechanical wave propagation. Tang et al.[22,23] established a quasi-static approach to relate the amount of the released energy in damage process to the event magnitude. In such methodologies, mechanical wave aspects like propagation and interactions with discontinuities, signal attenuation, reflection and coalescence may not be included. As an attempt in trying to partially address the existing shortcomings and gaps in the literature of induced AE and ME simulation, Komijani and his co-workers recently introduced enriched finite element methods[24,25] and numerical modelling approaches developed and tailored for simulation of the coupled process of localization-induced wave emissions in porous media with single-phase fluid flow in the cases of ME induced by shear-slip instability at pre-existing fractures[26] and tensile fracture propagation induced AE.[27]

This article presents a novel enriched mixed finite element formulation for fully coupled dynamic thermo-hydro-mechanical (THM) simulation of deformable fractured porous media with three-phase (water-gas-nonaqueous) fluid flow and thermal coupling. The governing equations are developed based on the generalized mixture theory of Biot.[28,29] Microseismicity induced by shear-slip instability, and tensile fracturing-induced AEs are simulated, and the effects of different system parameters on the induced wave signals are investigated.

2 | MATHEMATICAL FORMULATION

The governing equations of motion and the mas conservation equations for different phases are derived in the context of the generalized mixture theory of Biot based on the idea of volume fractions for different phases. The thermal (conductive

and convective heat transfer) coupling is governed by the thermal energy conservation equation for the total mixture with consideration of all the phases in a REV to be internally in thermal equilibrium condition resulting in the same temperature for all the phases at any material point of the mixture. Porous media is considered to be comprised of a deformable solid skeleton with pore spaces that are filled with different phases of fluids namely, gas (g), water (w) and a non-aqueous fluid (n) (e.g. petroleum hydrocarbons).

2.1 | Governing equations of multi-phase porous media with thermo-hydro-mechanical coupling

The domain of study is considered to be a two-dimensional poroelastic medium, Ω, in an orthogonal Cartesian coordinate O_{xy}. The primary variables are chosen to be the solid skeleton deformation, $\boldsymbol{u}(x, y, t)$, water phase pressure, $p_w(x, y, t)$, gaseous phase pressure, $p_g(x, y, t)$, non-aqueous phase fluid pressure, $p_n(x, y, t)$ and the temperature of the mixture, $T(x, y, t)$, with (t) denoting the time.

Considering the deformation to be infinitesimal, the strain–displacement relations are

$$\boldsymbol{\varepsilon} = \frac{1}{2}(\nabla \boldsymbol{u} + (\nabla \boldsymbol{u})^T) \tag{1}$$

The constitutive equation for the solid matrix relating the effective stress tensor to the strain tensor with consideration of the thermal strain contributions is given by

$$\boldsymbol{\sigma}' = \boldsymbol{C} : (\boldsymbol{\varepsilon} - \boldsymbol{I} \cdot \boldsymbol{\alpha} (T - T_0)) \tag{2}$$

in which $\boldsymbol{\sigma}'$ is the effective stress tensor acting on the solid skeleton, $\boldsymbol{C}$ is the elastic stiffness tensor, $\boldsymbol{I}$ is the identity tensor and $\boldsymbol{\alpha}$ is the thermal expansion tensor. T_0 is the initial equilibrium temperature used as a reference value to measure the temperature change induced thermal strain.

The relative velocity of fluid phases with respect to the solid skeleton is represented by $\dot{\boldsymbol{w}}_a$ ($a = w, g, n$). For loading conditions up to the earthquake frequencies, the relative acceleration of fluid phases with respect to the solid phase may be considered to be negligible, that is, $\ddot{\boldsymbol{w}}_a = 0$.[36] Therefore, in the motion equations of the fluid phase, the acceleration of fluid is considered to be equal to the acceleration of the total mixture (i.e. solid phase acceleration). Considering an REV of the solid-fluids system, and based on the concept of volume fractions, the motion equation for the total mixture may be written as

$$\nabla \cdot \boldsymbol{\sigma} - \rho_{av}\ddot{\boldsymbol{u}} + \rho_{av}\boldsymbol{b} = 0 \tag{3}$$

$\ddot{\boldsymbol{u}}$ is the acceleration of the mixture, $\boldsymbol{\sigma}$ is the total stress, ρ_{av} is the average density of the mixture and b denotes the body force (gravitational acceleration) acting on the mixture.

The average density of the mixture is defined as a weighted sum of solid and fluid phases densities where the weighting functions are the volume fractions of each of the phases:

$$\rho_{av} = n'(S_w\rho_w + S_g\rho_g + S_n\rho_n) + (1 - n')\rho_s \tag{4}$$

where ρ_w, ρ_g, ρ_n and ρ_s indicate, respectively, the density of the water, gas, non-aqueous and solid phases. n' denotes the porosity of the media defined as the ratio of the pore space volume to the total volume of the REV. S_w, S_g and S_n denote the degree of saturation for the water, gas and non-aqueous fluid phases, respectively. The degree of saturation for non-solid phases filling the pore space are defined as the ratio of the volume of the fluid phase to the total volume of the pore space and therefore, the following partition-of-unity (PU) relation holds between the saturations of different fluid phases:

$$S_w + S_g + S_n = 1 \tag{5}$$

The total stress of the mixture is defined as combination of the effective stress acting on the solid phase (stemming from the induced strain in the deformable solid) and the pore pressure:

$$\boldsymbol{\sigma} = \boldsymbol{\sigma}' - \alpha \bar{p} \boldsymbol{I} \tag{6}$$

in which $\bar{p}$ is the mean pore pressure, $\boldsymbol{\sigma}'$ denotes the effective stress acting on the solid skeleton and $\alpha = 1 - \frac{K_T}{K_S}$ (K_T and K_S being the bulk moduli of the porous medium and the solid grain, respectively) is the Biot's coefficient which is typically considered to be one. The mean pore pressure is defined as the weighted average of the pressures of different fluid phases as below:

$$\bar{p} = S_w p_w + S_g p_g + S_n p_n \tag{7}$$

The generalized Darcy relation can be deduced from conservation of momentum for each fluid phase as below, assuming the zero relative acceleration of the fluid phases with respect to the solid:

$$-\nabla p_a - \boldsymbol{R}_a - \rho_a \ddot{\boldsymbol{u}} + \rho_a \boldsymbol{b} = 0 \tag{8}$$

$\boldsymbol{R}_a$ is the lumped viscous drag acting on the fluid phase a ($a = w, g, n$) which is defined by the Darcy seepage law as

$$\dot{\boldsymbol{w}}_a = \boldsymbol{k}_a \boldsymbol{R}_a \tag{9}$$

where $\boldsymbol{k}_a$ is the permeability tensor of the porous medium to the pore fluid a defined as

$$\boldsymbol{k}_a = \boldsymbol{k} \frac{k_{ra}}{\mu_a} \tag{10}$$

In which $\boldsymbol{k}$ is the intrinsic permeability tensor of the porous medium (typically considered to be dependent on the pore space structure/size), $0 \leqslant k_{ra}(S_a) \leqslant 1$ is the relative permeability of the fluid phase (considered to be a function of the fluid saturation), and μ_a is the dynamic viscosity of the fluid phase a.

With consideration of the concept of volume fractions for different phases in an REV, the mass conservation equation of the fluid phases in the Eulerian description may be represented as

$$\frac{d}{dt}(\rho_a S_a n') + \nabla \cdot (\rho_a \dot{\boldsymbol{w}}_a) = 0 \tag{11}$$

In a similar fashion, the mass conservation of the solid phase may be written as

$$\frac{d}{dt}[\rho_s(1 - n')] + \nabla \cdot (\rho_s \dot{\boldsymbol{u}}) = 0 \tag{12}$$

The density of the fluid phases is considered to be a function of temperature and fluid pressure defined by the following relation as described by Fernandez[41]:

$$\rho_a = \rho_{a0} \, exp \left[-\beta_a (T_a - T_0) + \frac{p_a - p_0}{K_a} \right] \tag{13}$$

where β_a and K_a are the volumetric thermal expansion coefficient and the bulk moduli of the fluid phase a, respectively. T_0 and p_0 are the reference temperature and pressure, respectively. Similarly, the density of the solid phase is considered to be a function of the temperature, mean pore pressure and the first invariant of the effective stress tensor (i.e. hydrostatic stress).

The saturation of each fluid phase is considered to be a function of the capillary pressures of gas–water (p_{cgw}) and non-aqueous fluid–water (p_{cnw}) systems defined below:

$$p_{cgw} = p_g - p_w, \quad p_{cnw} = p_n - p_w, \quad p_{cgn} = p_g - p_n = p_{cgw} - p_{cnw} \tag{14}$$

The distribution of zones in gas–water-non-aqueous fluid system depends on the capillary pressures, and may be defined as below[46]:
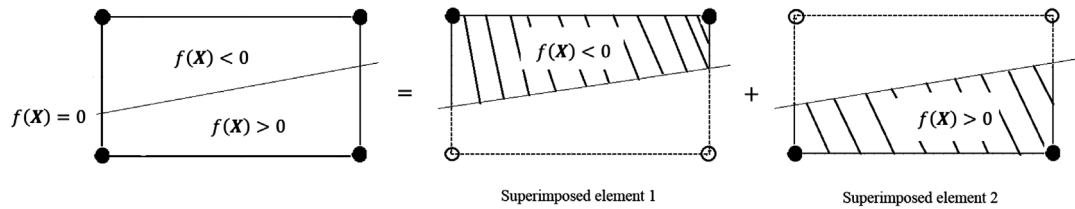
FIGURE 1 Substitution of a cracked element with two intact/regular superimposed paired elements with original real and additional phantom nodes in the framework of the PNM. Original real nodes and additional phantom nodes are depicted by solid and hollow circles, respectively. The shaded portion of each superimposed element represents the active part of those elements.[26].
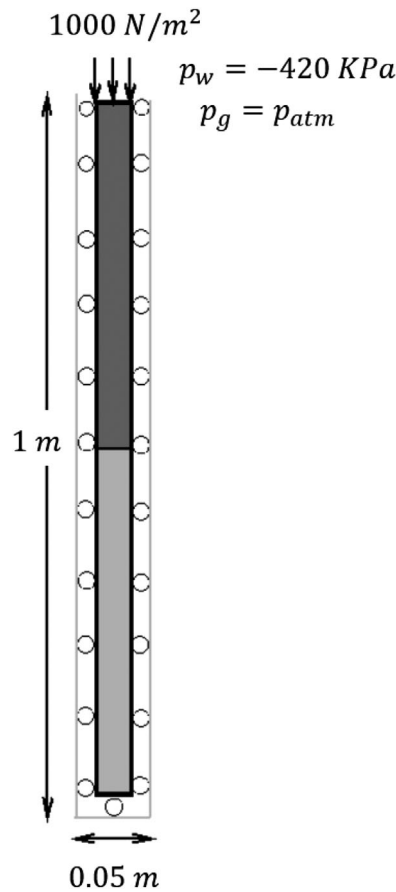

FIGURE 2 Schematic figure of the geometry and boundary conditions of the bimaterial soil column of Section 5.1.1.

I: Water only $[p_{cgw} \leq p_{dgw}, \ p_{cnw} \leq p_{dnw}]$

$$S_w = 1 \tag{15}$$

II: Water and gas $[p_{cgw} > p_{dgw}]$

$$S_w = S_{max} \left[\frac{p_{dgw}}{p_{cgw}} \right]^{\lambda} + S_{rw}, \quad S_w + S_g = 1 \tag{16}$$

III: Water and non-aqueous $[p_{cnw} > p_{dnw}], \ [p_{cgn} \leq p_{dgn}]$

$$S_w = S_{max} \left[\frac{p_{dnw}}{p_{cnw}} \right]^{\lambda} + S_{rw}, \quad S_w + S_n = 1 \tag{17}$$

TABLE 1 Material properties of the soil column of Section 5.1.1.

Poisson ratio	$\nu = 0.4$
Biot constant	$\alpha = 1$
Porosity	$n' = 0.3$
Solid density	$\rho_s = 2000 \; kg/m^3$
Water density	$\rho_w = 1000 \; kg/m^3$
Gas density	$\rho_g = 1.22 \; kg/m^3$
Bulk modulus of solid	$K_s = 0.14 \times 10^{10} \; Pa$
Bulk modulus of water	$K_w = 0.43 \times 10^{13} \; Pa$
Bulk modulus of gas	$K_g = 0.1 \times 10^6 \; Pa$
Intrinsic permeability	$\boldsymbol{k} = 0.46 \times 10^{-11} \; m^2$
Dynamic viscosity of water	$\mu_w = 1 \times 10^{-3} \; Pa \cdot s$
Dynamic viscosity of gas	$\mu_g = 1 \times 10^{-3} \; Pa \cdot s$
Volumetric thermal expansion coefficient	$\beta = 9 \times 10^{-8} \; 1/^0C$
Solid specific heat	$C_s = 878 \; J/kg^0C$
Water specific heat	$C_w = 4184 \; J/kg^0C$
Gas specific heat	$C_g = 1000 \; J/kg^0C$
Heat conductivity of the bulk	$\kappa = 837 \; W/m^0C$
Gravitational acceleration	$g = 9.806 \; m/s^2$
Atmpspheric pressure	$p_{atm} = 101.89 \; kPa$

IV: Water, gas and non-aqueous $[p_{cnw} > p_{dnw}]$, $[p_{cgn} > p_{dgn}]$

$$S_w = S_{max} \left[\frac{p_{dnw}}{p_{cnw}} \right]^\lambda + S_{rw}, \quad S_n = S_{max} \left(\left[\frac{p_{dgn}}{p_{cgn}} \right]^\lambda - \left[\frac{p_{dnw}}{p_{cnw}} \right]^\lambda \right) + S_{rn}, \quad S_g = 1 - S_w - S_n \tag{18}$$

The constant porous mixture properties in the above capillary pressures varying saturation functions are prescribed below:
$S_{max} = 1 - S_{rw} - S_{rn} - S_{rg}$, with S_{rw}, S_{rg}, S_{rn} being the residual saturations of water, gas and the non-aqueous fluid phases, respectively. It is noted that the residual saturation of the non-wetting phase (i.e. gas) is usually considered to be zero. λ is a pore size distribution index. p_{dgw} is the displacement pressure for gas–water system, p_{dnw} is the displacement pressure for non-aqueous fluid–water system and p_{dgn} is the displacement pressure for gas–non-aqueous fluid system.

The relative permeabilities of fluid phases (see Equation 10) may be expressed as functions of fluid saturations[42,43]:

$$k_{rw} = S_{ew}^{\left(\frac{2+3\lambda}{\lambda} \right)}, \quad k_{rg} = (1 - S_{te})^2 (1 - S_{te}^{\left(\frac{2+\lambda}{\lambda} \right)}) \quad k_{rn} = (S_{te} - S_{ew})^2 \left(S_{te}^{\left(\frac{2+\lambda}{\lambda} \right)} - S_{ew}^{\left(\frac{2+\lambda}{\lambda} \right)} \right) \tag{19}$$

where, $S_{ew} = (S_w - S_{rw})/S_{max}$ and $S_{te} = (1 - S_g - S_{rw} - S_{rn})/S_{max}$

The mass conservation equation of each pore fluid phase may be written in a distributed form based on Equation (11) and using Equation (13) with consideration of saturations as functions of the capillary pressures ($S_a = f(p_{cgw}, p_{cnw})$).

$$-n' S_w \beta_w \dot{T} + \frac{n' S_w}{K_w} \dot{p}_w + n' \frac{\partial S_w}{\partial p_{cgw}} \dot{p}_g + n' \frac{\partial S_w}{\partial p_{cnw}} \dot{p}_n - n' \left(\frac{\partial S_w}{\partial p_{cgw}} + \frac{\partial S_w}{\partial p_{cnw}} \right) \dot{p}_w + \nabla \cdot \dot{\boldsymbol{w}}_w = 0 \tag{20}$$

$$-n' S_g \beta_g \dot{T} + \frac{n' S_g}{K_g} \dot{p}_g - n' \left(\frac{\partial S_w}{\partial p_{cgw}} + \frac{\partial S_n}{\partial p_{cgw}} \right) \dot{p}_g - n' \left(\frac{\partial S_w}{\partial p_{cnw}} + \frac{\partial S_n}{\partial p_{cnw}} \right) \dot{p}_n$$

$$+ n' \left(\frac{\partial S_w}{\partial p_{cgw}} + \frac{\partial S_n}{\partial p_{cgw}} + \frac{\partial S_w}{\partial p_{cnw}} + \frac{\partial S_n}{\partial p_{cnw}} \right) \dot{p}_w + \nabla \cdot \dot{\boldsymbol{w}}_g = 0 \tag{21}$$

$$-n' S_n \beta_n \dot{T} + \frac{n' S_n}{K_n} \dot{p}_n + n' \frac{\partial S_n}{\partial p_{cgw}} \dot{p}_g + n' \frac{\partial S_n}{\partial p_{cnw}} \dot{p}_n - n' \left(\frac{\partial S_n}{\partial p_{cgw}} + \frac{\partial S_n}{\partial p_{cnw}} \right) \dot{p}_w + \nabla \cdot \dot{\boldsymbol{w}}_n = 0 \tag{22}$$

Equations (20)–(22) are the mass conservation equations for the water, gas and non-aqueous fluid phases, respectively.
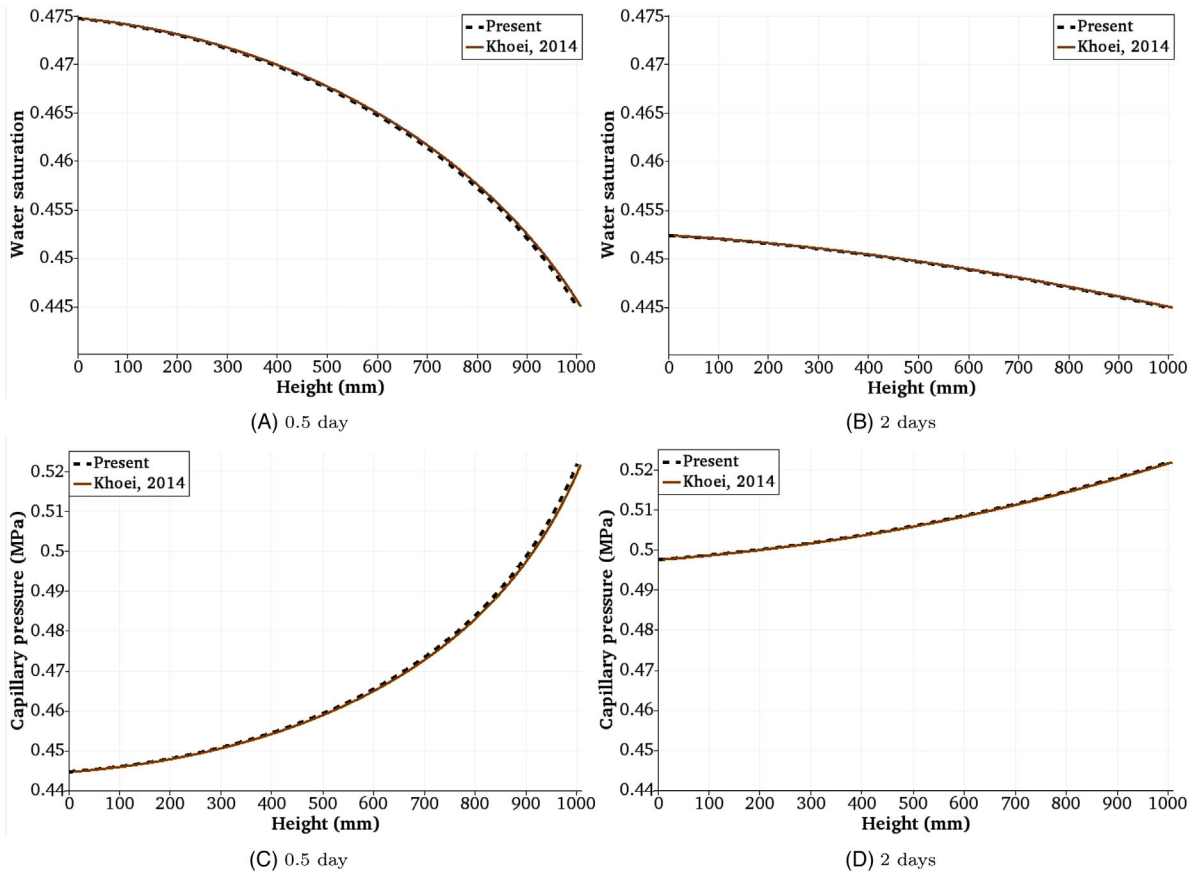
FIGURE 3   Comparison studies on variations with the column height.

The mass conservation of the solid phase may be developed in a similar fashion as

$$-(\alpha - n')\beta_s \dot{T} + \left(S_w - \left(\frac{\partial S_w}{\partial p_{cnw}} + \frac{\partial S_w}{\partial p_{cgw}} \right)(p_w - p_g) - \left(\frac{\partial S_n}{\partial p_{cnw}} + \frac{\partial S_n}{\partial p_{cgw}} \right)(p_n - p_g) \right)\frac{\alpha - n'}{K_s}\dot{p}_w$$

$$+ \left(S_n + \frac{\partial S_w}{\partial p_{cnw}}(p_w - p_g) + \frac{\partial S_n}{\partial p_{cnw}}(p_n - p_g) \right)\frac{\alpha - n'}{K_s}\dot{p}_n +$$

$$\left((1 - S_w - S_n) + \frac{\partial S_w}{\partial p_{cgw}}(p_w - p_g) + \frac{\partial S_n}{\partial p_{cgw}}(p_n - p_g) \right)\frac{\alpha - n'}{K_s}\dot{p}_g + \alpha\nabla \cdot \dot{\boldsymbol{u}} = 0 \qquad (23)$$

where β_s and K_s are the volumetric thermal expansion coefficient and the bulk moduli of the solid phase, respectively.

The continuity equations for the flow of the three fluid phases through the deformable solid matrix can be written as follows with substitution of the relative fluid velocity using the Darcy's seepage law (9):

$$\sum_{i\in\{w,g,n\}} \left(\frac{\dot{p}_i}{Q_{ki}} \right) + \beta_{kT}\dot{T} + \nabla \cdot (\boldsymbol{k}_k(-\nabla p_k + \rho_k \boldsymbol{b} - \rho_k \ddot{\boldsymbol{u}})) + S_k \alpha \nabla \cdot \dot{\boldsymbol{u}} = 0 \quad for \ \ k = \{w, g, n\} \qquad (24)$$

The compressibility (Q_{ki}) and the volumetric thermal expansion coefficients (β_{kT}) in the above continuity equations (24) are given in Appendix A.

The thermal energy conservation equation for an arbitrary REV with differential volume ($dV = dxdydz$) comprising a solid matrix with pore spaces filled with water, gas and non-aqueous fluid may be denoted as

$$\frac{\partial}{\partial t}(m_s C_s T) + \frac{D}{Dt}\big((m_w C_w T) + (m_g C_g T) + (m_n C_n T)\big) = (q_x^T - q_{x+dx}^T)(dy\ dz)$$

$$+ (q_y^T - q_{y+dy}^T)(dx\ dz) + (q_z^T - q_{z+dz}^T)(dx\ dy) \qquad (25)$$
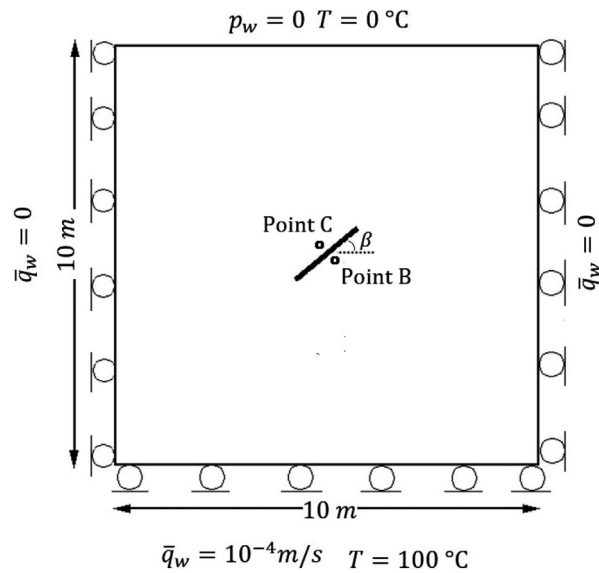
FIGURE 4 Schematic figure of the geometry and boundary conditions of the fractured porous medium of Section 5.1.2.

TABLE 2 Material properties of the porous medium of Section 5.1.2.

|	
Youngs modulus	$E = 6 \times 10^3 \ kPa$
Poisson ratio	$\nu = 0.4$
Biot constant	$\alpha = 1$
Porosity	$n' = 0.3$
Solid density	$\rho_s = 2000 \ kg/m^3$
Water density	$\rho_w = 1000 \ kg/m^3$
Bulk modulus of solid	$K_s = 1 \times 10^{14} \ MPa$
Bulk modulus of water	$K_w = 2 \times 10^3 \ MPa$
Intrinsic permeability	$\boldsymbol{k} = 1.1 \times 10^{-12} \ m^2$
Dynamic viscosity of water	$\mu_w = 1 \times 10^{-3} \ Pa \cdot s$
Volumetric thermal expansion coefficient	$\beta = 9 \times 10^{-8} \ 1/^0C$
Solid specific heat	$C_s = 878 \ J/kg^0C$
Water specific heat	$C_w = 4184 \ J/kg^0C$
Heat conductivity of the bulk	$\kappa = 837 \ W/m^0C$
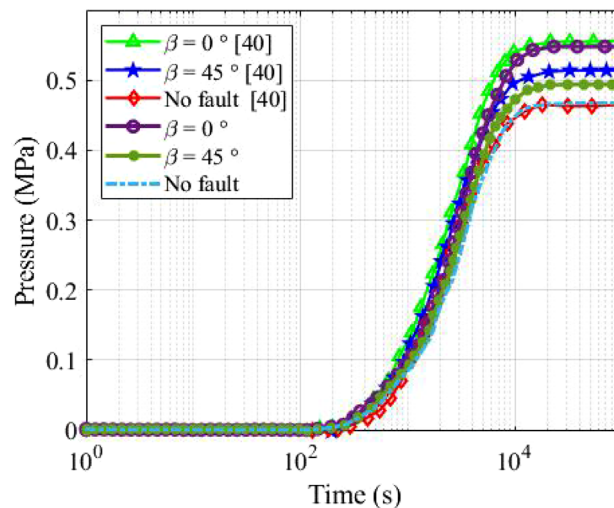
FIGURE 5 Time histories of water pressure in different continuous and fractured domains.

in which m_a and C_a with the corresponding subscripts ($a = s, w, g, n$) denote, respectively, the mass and the specific heat of the components: solid phase (s), water phase (w), gas phase (g) and the non-aqueous phase (n). In the above enthalpy balance equation $(q_x^T - q_{x+dx}^T)$, $(q_y^T - q_{y+dy}^T)$ and $(q_z^T - q_{z+dz}^T)$ are the net heat conduction fluxes into the REV in x, y and z directions, respectively.

The thermal energy conservation equation may be expanded by substituting for the mass components in Equation (25) based on the densities of different phases and the corresponding volumes in the REV based on the porosity and the degrees of saturation:

$$\frac{\partial}{\partial t}\left(\rho_s(1-n')(dV)C_sT\right) + \frac{D}{Dt}\left(\sum_{i\in\{w,g,n\}}\left(\rho_i n'(dV)S_iC_i\right)T\right)$$

$$= (q_x^T - q_{x+dx}^T)(dy\,dz) + (q_y^T - q_{y+dy}^T)(dx\,dz) + (q_z^T - q_{z+dz}^T)(dx\,dy) \tag{26}$$

Dividing both sides of Equation (26) by the differential volume (dV) and taking derivatives with respect to time in the left side and using the Fourier's law of heat conduction ($\boldsymbol{q}^T = -\boldsymbol{\kappa}\nabla T$), the differential form of the thermal energy conservation equation may be developed as

$$\left(\rho_s(1-n')C_s\dot{T}\right) + \sum_{i\in\{w,g,n\}}\left(\frac{D}{Dt}\left(\rho_i(n')S_iC_iT\right)\right) = \nabla\cdot(\boldsymbol{\kappa}_{av}\nabla T) \tag{27}$$

$\boldsymbol{\kappa}_{av} = (1-n')\boldsymbol{\kappa}_s + \sum_{i\in\{w,g,n\}}((n'S_i)\boldsymbol{\kappa}_i)$ is the heat conductivity tensor of the mixture, with $\boldsymbol{\kappa}_a$ ($a = s, w, g, n$) being the conductivity tensors for the solid, water, gas and the non-aqueous phases. With consideration of the time derivative of temperature in the Eulerian description ($\frac{DT}{Dt} = \dot{T} + \nabla T\cdot\boldsymbol{w}_i, i = w, g, n$) for the flowing fluid phases, Equation (27) may be written as[46]:

$$\left(\rho_s(1-n')C_s + \sum_{i\in\{w,g,n\}}\left(\rho_i(n')S_iC_i\right)\right)\dot{T} + \left(\sum_{i\in\{w,g,n\}}\left(\rho_i\dot{\boldsymbol{w}}_iC_i\right)\right)\nabla T - \nabla\cdot(\boldsymbol{\kappa}_{av}\nabla T) = 0 \tag{28}$$

The second term in Equation (28) indicates the effect of the fluid mass transfer (manifested by the fluid flow velocity, $\dot{\boldsymbol{w}}_i$ in the form of advection) through the boundaries of the control volume in the heat balance equation as a convection term.[40,46]

The relative velocities of the fluid phases with respect to the mixture can be eliminated from the thermal energy conservation equations (28) considering the Darcy's seepage law (9), resulting in the following version of the mixture enthalpy balance equation represented in terms of displacement, temperature and fluid pressures variables.

$$\left(\rho_s(1-n')C_s + \rho_w(n')S_wC_w + \rho_n(n')S_nC_n + \rho_g(n')(1-S_w-S_n)C_g\right)\dot{T}$$

$$+ \left(\rho_wC_w\left(\boldsymbol{k}_w(-\nabla p_w + \rho_w\boldsymbol{b} - \rho_w\ddot{\boldsymbol{u}})\right) + \rho_gC_g\left(\boldsymbol{k}_g(-\nabla p_g + \rho_g\boldsymbol{b} - \rho_g\ddot{\boldsymbol{u}})\right)\right.$$

$$\left. + \rho_nC_n\left(\boldsymbol{k}_n(-\nabla p_n + \rho_n\boldsymbol{b} - \rho_n\ddot{\boldsymbol{u}})\right)\right)\nabla T - \nabla\cdot(\boldsymbol{\kappa}_{av}\nabla T) = 0 \tag{29}$$

2.2 | Weak formulation of the governing differential equations

In order to obtain the unknown primary variables, namely, the solid skeleton deformation, $\boldsymbol{u}(x, y, t)$, water phase pressure, $p_w(x, y, t)$, gaseous phase pressure, $p_g(x, y, t)$, non-aqueous phase fluid pressure, $p_n(x, y, t)$ and the temperature of the mixture, $T(x, y, t)$, the motion equation of the mixture (3) needs to be solved coupled with the fluid continuity equations (24), and the thermal energy conservation equation (29).

Porous medium Ω with boundary Γ is considered in O_{xy} with $\boldsymbol{n}_\Gamma$ being the unit normal vector to the boundary surface. The boundary Γ comprises the complementary essential and natural boundary conditions defined over the corresponding parts of the boundary surface: Γ_u and Γ_t ($\Gamma_u \cup \Gamma_t = \Gamma$) representing the boundary surfaces for prescribed displacement ($\boldsymbol{u} = \bar{\boldsymbol{u}}$) and traction ($\bar{\boldsymbol{t}} = \boldsymbol{\sigma}\cdot\boldsymbol{n}_{\Gamma_t}$), respectively; Γ_{p_w} and Γ_{q_w} ($\Gamma_{p_w} \cup \Gamma_{q_w} = \Gamma$) denoting the boundary surfaces for prescribed pressure ($p_w = \bar{p}_w$) and the out-flow flux of water phase ($\bar{q}_w = \dot{\boldsymbol{w}}_w\cdot\boldsymbol{n}_{\Gamma_{q_w}}$), respectively; Γ_{p_g} and Γ_{q_g} ($\Gamma_{p_g} \cup \Gamma_{q_g} = \Gamma$) denoting the boundary surfaces for prescribed pressure ($p_g = \bar{p}_g$) and the out-flow flux of the gaseous phase ($\bar{q}_g = \dot{\boldsymbol{w}}_g\cdot\boldsymbol{n}_{\Gamma_{q_g}}$),

respectively; Γ_{p_n} and Γ_{q_n} ($\Gamma_{p_n} \cup \Gamma_{q_n} = \Gamma$) indicating the boundary surfaces for prescribed pressure ($p_n = \bar{p}_n$) and the out-flow flux of the nonaqueous phase ($\bar{q}_n = \dot{\boldsymbol{w}}_n \cdot \boldsymbol{n}_{\Gamma_{q_n}}$), respectively; Γ_T and Γ_{q_T} ($\Gamma_T \cup \Gamma_{q_T} = \Gamma$) denoting the boundary surfaces for prescribed temperature ($T = \bar{T}$) and the out-flow thermal flux ($\bar{q}_T = -\boldsymbol{\kappa}_{av}\nabla T \cdot \boldsymbol{n}_{\Gamma_{q_T}}$), respectively. The domain Ω contains internal interfaces (i.e. fractures) denoted by Γ_d. $\boldsymbol{n}_{\Gamma_d}$ is the unit normal vector to Γ_d pointing to Ω^+ with $\boldsymbol{n}_{\Gamma_d} = \boldsymbol{n}_{\Gamma_{d-}} = -\boldsymbol{n}_{\Gamma_{d+}}$, where superscripts $+$ and $-$ represent the two sides of the discontinuity.

The weak form of the coupled system of Equations (3), (24) and (29) may be developed by multiplying the equations by appropriate consistent test functions, $\delta\boldsymbol{u}$, δp_k ($k = \{w, g, n\}$), and δT, respectively, and integrating over the domain Ω, implementing the Divergence theorem. The problem is to be solved to find $\mathbf{u}(x, y, t) \in U$, $p_k(x, y, t) \in W_k$ ($k = \{w, g, n\}$) and $T(x, y, t) \in W_T$ such that

$$\int_\Omega \boldsymbol{\sigma} : \delta\boldsymbol{\varepsilon} \, d\Omega + \int_\Omega \rho_{av}\ddot{\boldsymbol{u}} \cdot \delta\boldsymbol{u} \, d\Omega - \int_{\Gamma_t} \bar{\boldsymbol{t}} \cdot \delta\boldsymbol{u} \, d\Gamma - \int_\Omega \rho_{av}\boldsymbol{b} \cdot \delta\boldsymbol{u} \, d\Omega + \int_{\Gamma_d} \bar{\boldsymbol{t}_d} \cdot \delta[[\boldsymbol{u}]] \, d\Gamma = 0, \forall\delta\boldsymbol{u} \in U_0 \tag{30}$$

$$\sum_{i \in \{w,g,n\}} \left(\int_\Omega \delta p_k \left(\frac{\dot{p}_i}{Q_{ki}} \, d\Omega \right) \right) + \int_\Omega \delta p_k \, \beta_{kT} \, \dot{T} \, d\Omega$$

$$+ \int_\Omega S_k \delta p_k \, \alpha \, \nabla \cdot \dot{\boldsymbol{u}} \, d\Omega + \int_\Omega \nabla\delta p_k \cdot \boldsymbol{k}_k \nabla p_k \, d\Omega$$

$$+ \int_\Omega \nabla\delta p_k \cdot (\boldsymbol{k}_k\rho_k)\ddot{\boldsymbol{u}} \, d\Omega - \int_\Omega \nabla\delta p_k \cdot (\boldsymbol{k}_k\rho_w)\boldsymbol{b} \, d\Omega$$

$$+ \int_{\Gamma_{q_k}} \delta p_k(\bar{q}_k) \, d\Gamma - \int_{\Gamma_d} \delta p_k[[\dot{\boldsymbol{w}}_k]] \cdot \boldsymbol{n}_{\Gamma_d} \, d\Gamma = 0, \forall\delta p_k \in W_{k_0} \ \ for \ \ k = \{w, g, n\} \tag{31}$$

$$\int_\Omega \delta T\big(\rho_s(1 - n')C_s + \rho_w(n')S_wC_w + \rho_n(n')S_nC_n + \rho_g(n')(1 - S_w - S_n)C_g\big)\dot{T} \, d\Omega$$

$$+ \int_\Omega \delta T \left(\rho_wC_w(\boldsymbol{k}_w(-\nabla p_w + \rho_w\boldsymbol{b} - \rho_w\ddot{\boldsymbol{u}})) + \rho_gC_g\big(\boldsymbol{k}_g(-\nabla p_g + \rho_g\boldsymbol{b} - \rho_g\ddot{\boldsymbol{u}})\big) \right.$$

$$\left. + \rho_nC_n(\boldsymbol{k}_n(-\nabla p_n + \rho_n\boldsymbol{b} - \rho_n\ddot{\boldsymbol{u}}))) \nabla T \, d\Omega \right.$$

$$+ \int_\Omega \nabla\delta T \cdot \boldsymbol{\kappa}_{av}\nabla T \, d\Omega + \int_{\Gamma_{q_T}} \delta T \, (\bar{q}_T) \, d\Gamma - \int_{\Gamma_d} \delta T[[-\boldsymbol{\kappa}_{av}\nabla T]] \cdot \boldsymbol{n}_{\Gamma_d} \, d\Gamma = 0, \forall\delta T \in W_{T_0} \tag{32}$$

where U, W_k ($k = \{w, g, n\}$), W_T, U_0, W_{k_0} ($k = \{w, g, n\}$) and W_{T_0} are appropriate function spaces. $[[\boldsymbol{u}]]$ denotes the jump in the displacement field across the discontinuity surface, $[[\dot{\boldsymbol{w}}_k]] \cdot \boldsymbol{n}_{\Gamma_d}$ ($k = w, g, n$) is the discontinuity of fluid flux into the crack interface from either crack face and $[[-\boldsymbol{\kappa}_{av}\nabla T]] \cdot \boldsymbol{n}_{\Gamma_d}$ represents the discontinuity of the thermal flux across the discontinuity surface. $\bar{\boldsymbol{t}_d}$ is the internal surface traction (e.g. contact force, cohesive force, hydraulic pressure in HF) applied on the discontinuity faces Γ_d. It is noted that $\bar{\boldsymbol{t}}$ implies any type of external tractions imposed on the external boundaries such as mechanical forces and hydraulic pressures induced by pore fluid injection.

3 | FINITE ELEMENT MODEL

3.1 | Phantom Node Method

The discontinuity in displacement, pore pressures and temperature fields inside an element may be accommodated through the concept of The Phantom Node Method (PNM).[35] In this framework, a discontinuous interpolation of a variable inside a cracked element is achieved through replacement of the element with two complementary superimposed paired intact elements with original real nodes from the underlying element and additional phantom nodes, as depicted schematically in Figure 1.
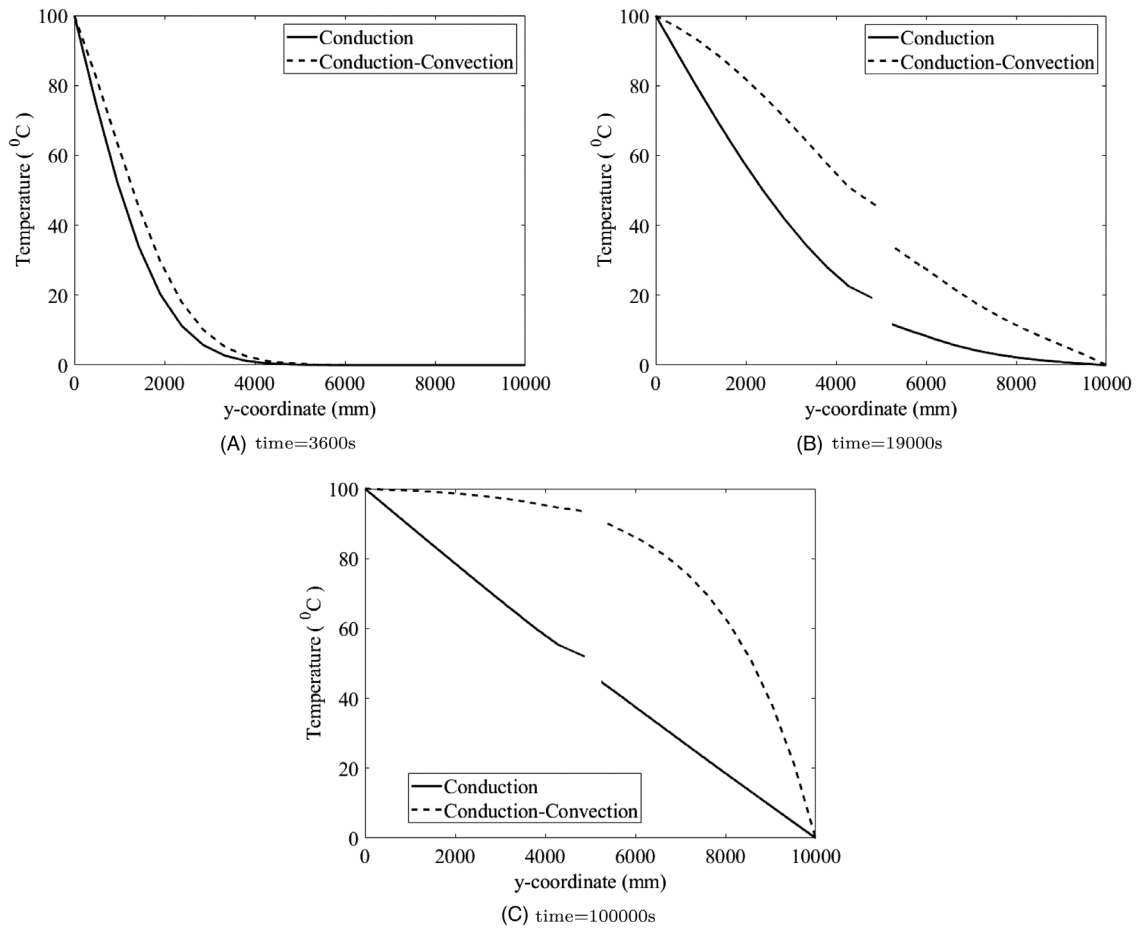
FIGURE 6 Temperature profiles through the *y*-axis at the middle of the domain along the line $x = 5m$ for conductive–convective and conductive heat transfer conditions.

3.1.1 | Finite element interpolations

For an element with internal impermeable insulated crack in a porous medium, finite element interpolation is used to approximate the displacement, pore pressures, and temperature fields. The finite element interpolation functions for the unknown variables Δ^β ($\beta = 1$ *through* 6) with $\Delta^1 = u_x, \Delta^2 = u_y, \Delta^3 = p_w, \Delta^4 = p_g, \Delta^5 = p_n, \Delta^6 = T$ may be represented as

$$\Delta^\beta(x, y, t) = H(-f(x, y)) \sum_{J \in S_1} \left(\psi_J^\beta(x, y) \Delta_J^\beta(t) \right) + H(f(x, y)) \sum_{J \in S_2} \left(\psi_J^\beta(x, y) \Delta_J^\beta(t) \right) \tag{33}$$

in which $H(\cdot)$ is the step function and S_1 and S_2 denote the sets of real and phantom nodes corresponding to each of the two superimposed elements. The geometry of the fracture within an element is determined by a level set function in such a way that $f(x, y) = 0$ represents the discontinuous surface, and $f(x, y) > 0$ and $f(x, y) < 0$ specify the two mutually exclusive sides of the fracture (the active parts of the superimposed elements 1 and 2). ψ_J^β represents the arrays of basis functions of a typical node J for the variables. Vectors of the corresponding degrees of freedom for typical node J are indicated by Δ_J^β.

In case of fluid flow at the fracture interface (i.e. permeable crack faces), the pressure and temperature fields in cracked elements are continuous and thus, there is no need for the additional phantom nodes in the associated interpolation functions. It is noted that permeable crack faces does not result in flux discontinuity (weak discontinuity) across the fracture in the present model as there is no internal fluid flow inside the fracture and separate from the fluid flow in the surrounding porous medium. In the case of fluid flow inside the fracture aperture with having leak off (e.g. HF simulation), a weak discontinuity needs to be considered across the fracture interface by embedding appropriate enrichment basis function
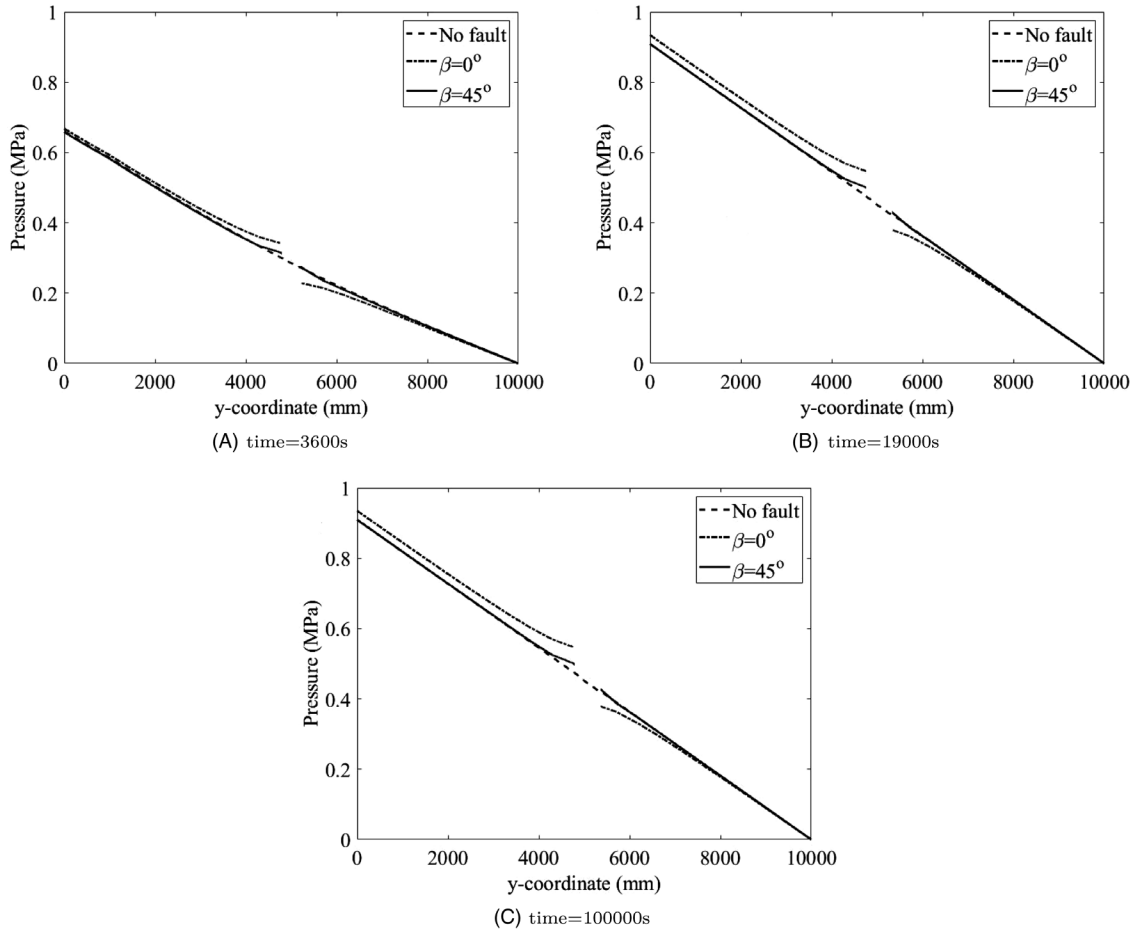
FIGURE 7 Water pressure profiles through the *y*-axis at the middle of the domain along the line $x = 5m$ for fractured and continuous media.

(see Moës et al.[47]). However, in the numerical examples of the present study, strong discontinuities have been considered for pressure and temperature fields similar to the displacement field, with zero fluid and thermal flux at interface.

3.2 | Discretized mixed finite element equations

Semi-discretized coupled system of finite element equations may be developed as follows by substituting for displacement, fluid pressures and temperature variables and their variations in Equations (30)–(32) using the finite element interpolation functions (33). It is noted that for each independent unknown variable, the same approximating spaces are used for trial and test functions.

$$\sum_{J=1}^{n_{node}} \left([M]_{IJ}^{\alpha\beta} \ddot{\boldsymbol{\Delta}}_J^\beta + [C]_{IJ}^{\alpha\beta} \dot{\boldsymbol{\Delta}}_J^\beta + [K]_{IJ}^{\alpha\beta} \boldsymbol{\Delta}_J^\beta \right) = \boldsymbol{F}_I^\alpha, \quad (I = 1, \dots, n_{node}) \tag{34}$$

In the above formulation, n_{node} denotes the maximum number of nodes (associated with the order of polynomials used for interpolation of different variables) in each of the two superposed paired elements 1 and 2, and includes both original real and additional phantom nodes. In an element cut by a crack, the definitions of $[M^e]_{IJ}^{\alpha\beta}$, $[C^e]_{IJ}^{\alpha\beta}$, $[K^e]_{IJ}^{\alpha\beta}$ and $\mathbf{F}_I^\alpha$ ($\alpha, \beta = 1 \text{ through } 6$) in Equation (34) for each of the superimposed elements, that is, $e = 1$ or 2, are provided in Appendix B.

To develop the fully discretized form of the finite element equations (34), the generalized Newmark implicit schemes are employed for time integration. The GN22 scheme is used for displacement and the GN11 is employed for fluid phases pore pressure as well as temperature degrees of freedom. In this framework, the unknown first- and second-order time
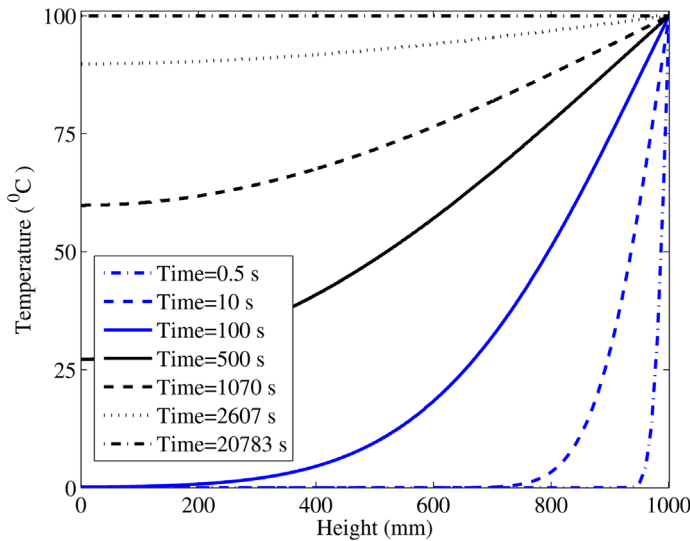
FIGURE 8 Through the height temperature profile of the soil column at different times.

derivatives of the variables at time step $(i + 1)$ are denoted in terms of the corresponding known values of the variables at the current time step (i) and unknown values of the variables at time step $(i + 1)$ as

$$\dot{p}_a^{(i+1)} = \frac{1}{\theta \Delta t}(p_a^{(i+1)} - p_a^{(i)}) - \left(\frac{1}{\theta} - 1\right)\dot{p}_a^{(i)}, \quad (a = w, g, n) \tag{35}$$

$$\dot{T}^{(i+1)} = \frac{1}{\theta_T \Delta t}(T^{(i+1)} - T^{(i)}) - \left(\frac{1}{\theta_T} - 1\right)\dot{T}^{(i)} \tag{36}$$

$$\dot{\boldsymbol{u}}^{(i+1)} = \frac{\gamma}{\beta \Delta t}(\boldsymbol{u}^{(i+1)} - \boldsymbol{u}^{(i)}) - \left(\frac{\gamma}{\beta} - 1\right)\dot{\boldsymbol{u}}^{(i)} - \Delta t\left(\frac{\gamma}{2\beta} - 1\right)\ddot{\boldsymbol{u}}^{(i)} \tag{37}$$

$$\ddot{\boldsymbol{u}}^{(i+1)} = \frac{1}{\beta \Delta t^2}\left(\boldsymbol{u}^{(i+1)} - \boldsymbol{u}^{(i)}\right) - \frac{1}{\beta \Delta t}\dot{\boldsymbol{u}}^{(i)} - \left(\frac{1}{2\beta} - 1\right)\ddot{\boldsymbol{u}}^{(i)} \tag{38}$$

in which γ, β, θ and θ_T are the time integration constants that are considered to be 0.7 in the numerical models of this work to assure the unconditional stability of the time integration.[40]

Due to the nonlinear nature of the coupled system of equations, an iterative non-linear solver needs to be designed and implemented to obtain the solution for vector of unknowns $\boldsymbol{\Delta}_J^\beta$ at each time step $(i + 1)$. In this work, the Newton–Raphson (NR) technique (see Reddy[44]) is implemented to linearize the non-linear system of equations and solve iteratively in each time step. After implementation of time integration using Equations (35), (36), (37) and (38), the set of coupled equations (34) renders six residual forms $\boldsymbol{R}_I^{\alpha(i+1)} = 0$ ($\alpha = 1$ through 6) as functions of six unknowns $\boldsymbol{\Delta}_J^{\beta(i+1)}$ ($\beta = 1$ through 6).

A linear approximation of the underlying non-linear system at time step $(i + 1)$ may be developed by the following first-order truncated Taylor series expansion of the residual equations:

$$\boldsymbol{R}_{I_{(n)}}^{\alpha(i+1)} = \boldsymbol{R}_{I_{(n-1)}}^{\alpha(i+1)} + \frac{\partial \boldsymbol{R}_{I_{(n-1)}}^{\alpha(i+1)}}{\partial \boldsymbol{\Delta}_{J_{(n-1)}}^{\beta(i+1)}}\delta\boldsymbol{\Delta}_{J_{(n)}}^{\beta(i+1)} = 0, \quad [T]_{IJ_{(n-1)}}^{\alpha\beta(i+1)} = \frac{\partial \boldsymbol{R}_{I_{(n-1)}}^{\alpha(i+1)}}{\partial \boldsymbol{\Delta}_{J_{(n-1)}}^{\beta(i+1)}} \tag{39}$$

The above linearized system of equations should be solved to obtain the incremental values of the unknown nodal degrees of freedom in each iteration n of the NR solution. Subsequently, the corresponding unknown nodal degrees of freedom can be sought by the following incremental relation:

$$\boldsymbol{\Delta}_{J_{(n)}}^{\beta(i+1)} = \boldsymbol{\Delta}_{J_{(n-1)}}^{\beta(i+1)} + \delta\boldsymbol{\Delta}_{J_{(n)}}^{\beta(i+1)}, \quad [T]_{IJ_{(n-1)}}^{\alpha\beta(i+1)}\delta\boldsymbol{\Delta}_{J_{(n)}}^{\beta(i+1)} = -\boldsymbol{R}_{I_{(n-1)}}^{\alpha(i+1)} \tag{40}$$
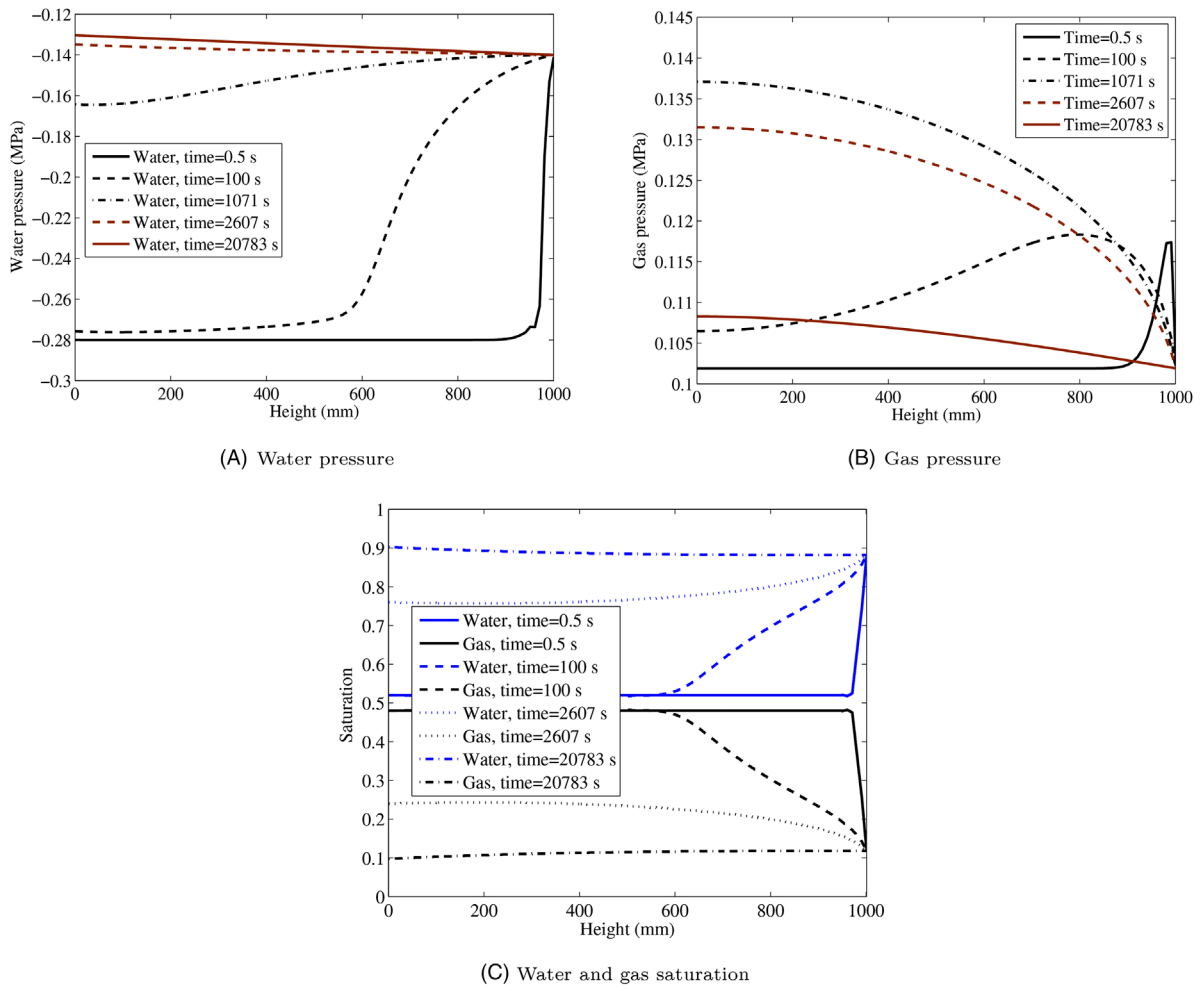
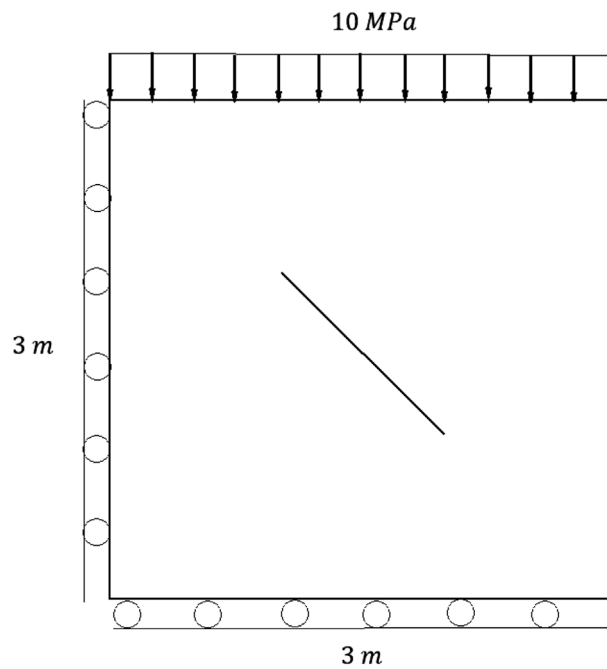**FIGURE 9**   Variations with the column height.

FIGURE 10   Schematic figure of the fractured porous medium studied in Section 5.3.

TABLE 3 Material properties of the porous medium of Section 5.3.

Youngs modulus	$E = 6 GPa$
Poisson ratio	$\nu = 0.3$
Biot constant	$\alpha = 1$
Porosity	$n' = 0.3$
Solid density	$\rho_s = 2000 \ kg/m^3$
Water density	$\rho_w = 1000 \ kg/m^3$
Gas density	$\rho_g = 0.5 \ kg/m^3$
Bulk modulus of solid	$K_s = 1 \times 10^{20} \ Pa$
Bulk modulus of water	$K_w = 2.15 \times 10^9 \ Pa$
Bulk modulus of gas	$K_g = 0.1 \times 10^6 \ Pa$
Intrinsic permeability	$\boldsymbol{k} = 0.29 \times 10^{-13} \ m^2$
Dynamic viscosity of water	$\mu_w = 1 \times 10^{-3} \ Pa \cdot s$
Dynamic viscosity of gas	$\mu_g = 8 \times 10^{-6} \ Pa \cdot s$
Volumetric thermal expansion coefficient of solid	$\beta_s = 3 \times 10^{-5} \ 1/^0C$
Volumetric thermal expansion coefficient of water	$\beta = 4 \times 10^{-4} \ 1/^0C$
Volumetric thermal expansion coefficient of gas	$\beta = 4 \times 10^{-3} \ 1/^0C$
Solid specific heat	$C_s = 878 \ J/kg^0C$
Water specific heat	$C_w = 4184 \ J/kg^0C$
Gas specific heat	$C_g = 1996 \ J/kg^0C$
Heat conductivity of solid	$\kappa_s = 2 \ W/m^0C$
Heat conductivity of water	$\kappa_w = 0.555 \ W/m^0C$
Heat conductivity of gas	$\kappa_g = 0.024 \ W/m^0C$
Gravitational acceleration	$b_y = 0 \ m/s^2$

4 | INTERFACE CONSTITUTIVE MODELLING

4.1 | Frictional contact modelling

Geological formations are under considerable in situ confining stresses due to overburden and horizontal tectonic stresses which may result in large frictional contact conditions along natural and induced discontinuities (fractures and faults). A series of research studies have been dedicated to development of numerically robust and stable computational framework for enforcing inter-facial conditions in contact.[37–39] In this work, an augmented Lagrange multiplier approach is implemented to enforce frictional contact constraints through an iterative procedure.

In existence of contact constraints at the interfaces of internal boundaries (strong discontinuities), the weak form of the mixture motion equation (30) may be written as below, with consideration of the contact traction contributions.

$$\int_\Omega \boldsymbol{\sigma} : \delta\boldsymbol{\varepsilon} \, d\Omega + \int_\Omega \rho\ddot{\boldsymbol{u}} \cdot \delta\boldsymbol{u} \, d\Omega - \int_{\Gamma_t} \bar{\boldsymbol{t}} \cdot \delta\boldsymbol{u} \, d\Gamma - \int_\Omega \rho\boldsymbol{b} \cdot \delta\boldsymbol{u} \, d\Omega - \int_{\Gamma_d} \bar{\lambda}_N \delta g_N d\Gamma$$

$$- \int_{\Gamma_d} \bar{\lambda}_T \delta g_T d\Gamma = 0 \qquad (41)$$

with $\bar{\lambda}_N$, g_N, $\bar{\lambda}_T$ and g_T being the interface contact traction, the penetration in normal direction, the friction traction tangent to the interface and the tangential displacement jump across the interface, respectively.

The normal and tangential components of contact traction are represented as Lagrange multiplier fields interpolated over the interface using one-dimensional elements along the discontinuity as

$$\bar{\lambda}_N = \tilde{\boldsymbol{N}}\bar{\boldsymbol{\lambda}}_N \text{ and } \bar{\lambda}_T = \tilde{\boldsymbol{N}}\bar{\boldsymbol{\lambda}}_T \qquad (42)$$

in which $\tilde{\boldsymbol{N}}$ are linear one-dimensional Lagrangian shape functions and $(\bar{\boldsymbol{\lambda}}_N, \bar{\boldsymbol{\lambda}}_T)$ are the vectors of Lagrange multipliers degrees of freedom. The gridding of the Lagrange multiplier field elements is performed using the Vital Vertex method.[38,39]
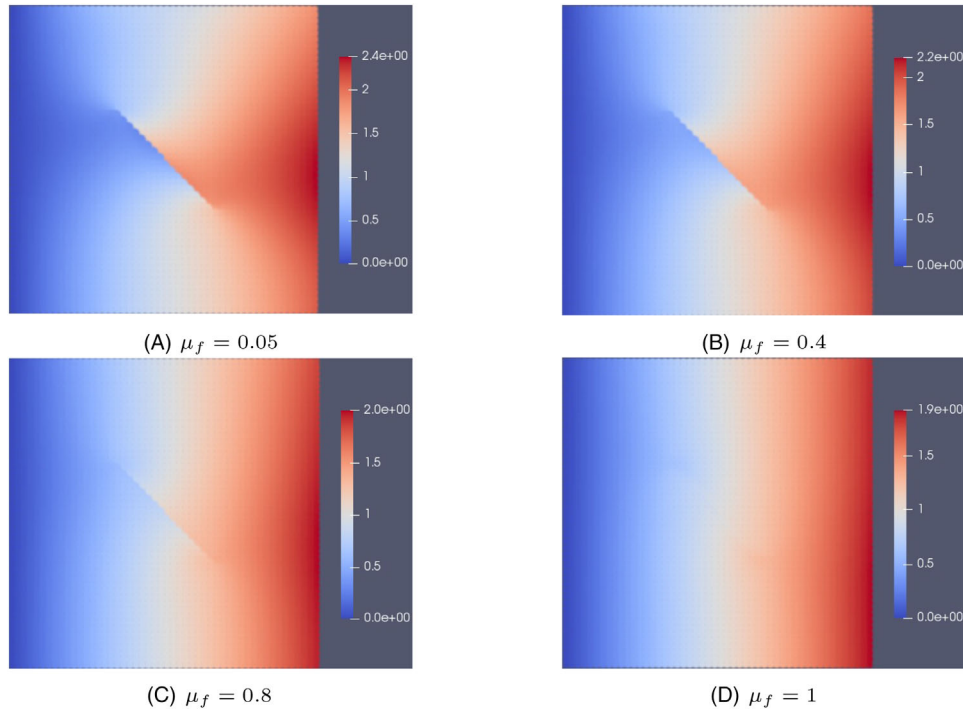
FIGURE 11 x-displacement (u_x in mm) contours for various friction coefficient values.

At each time step, the unknowns and $(\bar{\lambda}_N, \bar{\lambda}_T)^{(i+1)}$ are sought through a sequential successive substitution procedure. This process starts with ($k = 0$) given an initial guess for the vector of Lagrange multipliers $(\bar{\lambda}_N, \bar{\lambda}_T)^{(i+1)}_{k=0} = (\bar{\lambda}_N, \bar{\lambda}_T)^{(i)}$. Given $(\bar{\lambda}_N, \bar{\lambda}_T)^{(i+1)}_k$ at iteration k, the governing coupled system of equations is solved to get Δ_k^{i+1}, and from the solution the interpenetration g_{N_k} and tangential slip g_{T_k} at each grid point of the Lagrange multiplier mesh are computed. If the penetration g_{N_k} is greater than a prescribed tolerance, then the Lagrange multiplier nodal vector (normal contact tractions) needs to be updated using

$$\bar{\lambda}_{N_{(k+1)}} = \bar{\lambda}_{N_k} + d\bar{\lambda}_{N_k}, \quad and \quad d\bar{\lambda}_{N_k} = K_N g_{N_k} \tag{43}$$

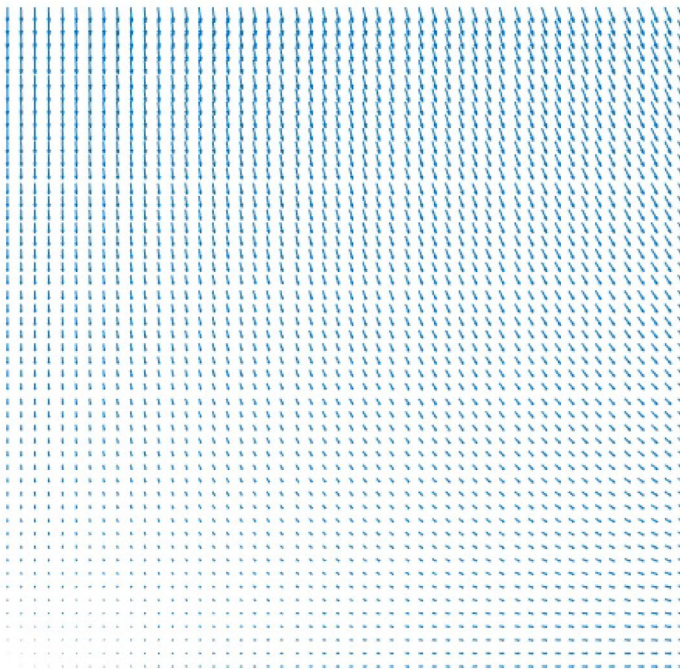in which K_N is an arbitrary rebounding stiffness value.

For the frictional component of contact traction, an analogous procedure is implemented to impose the contact constraint and obtain the frictional Lagrange multipliers at interface grid points. If the obtained tangential Lagrange multiplier $\bar{\lambda}_T$ exceeds the limit of $\bar{\lambda}_T^{max} = \bar{\lambda}_N \mu_f$ the interface is in slip condition; otherwise the stick condition is preserved ($g_T = 0$). For more detailed representation of the enriched finite element formulation of the frictional contact model, one may refer to Refs. 48, 49

4.2 | Cohesive fracture modelling

To model the damage behaviour at the crack-tip region in fracture propagation, the concept of cohesive fracture[30–32] is used. In this regard, a constitutive interface model is implemented in the fracture process zone based on defining the cohesive traction as a decaying function of the fracture opening.

$$\bar{t}_{coh} \cdot n = \sigma_u - \frac{\sigma_u}{\delta_u}[[u]] \cdot n \qquad if \qquad 0 < [[u]] \cdot n \leqslant \delta_u \tag{44}$$

in which $\bar{t}_{coh}$ is the cohesive interface traction, $[[u]]$ is the fracture opening through the stress degradation process, σ_u is the ultimate cohesive strength (at the start of fracturing process), δ_u is the ultimate cohesive separation (at the end of fracturing process) and n is the normal unit vector at the interface.

FIGURE 12 Displacement vector plots for various friction coefficient values.
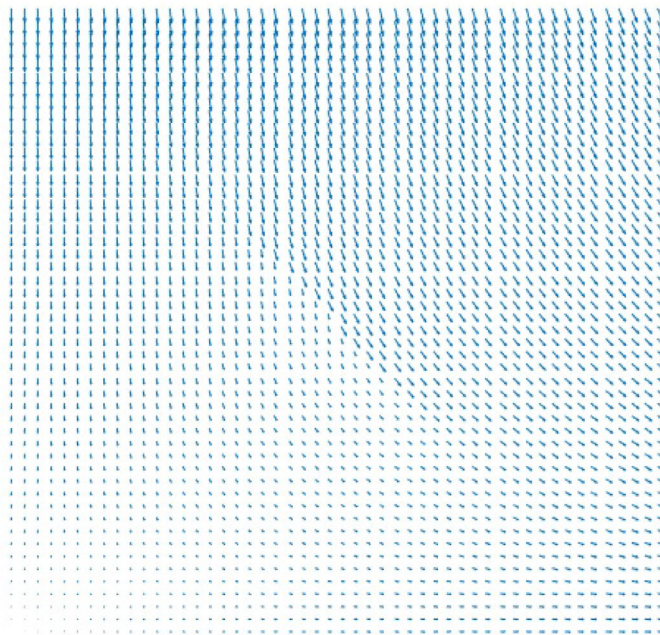
(A) $\mu_f = 0.05$, slip condition

(B) $\mu_f = 1$, stick condition

The energy dissipated due to cohesive tractions in a fracturing process is equal to the fracture energy, G_F:

$$G_F = \frac{1}{2}(\sigma_u \delta_u) \tag{45}$$

In order to characterize the brittleness, Carpinteri[33] introduced a non-dimensional number:

$$s_E = \frac{G_F}{\sigma_u b} \tag{46}$$

where b is related to the structure size. Bazant and Planas[34] suggested to call the mentioned parameter the ductility number, with larger s_E demonstrating more ductility.
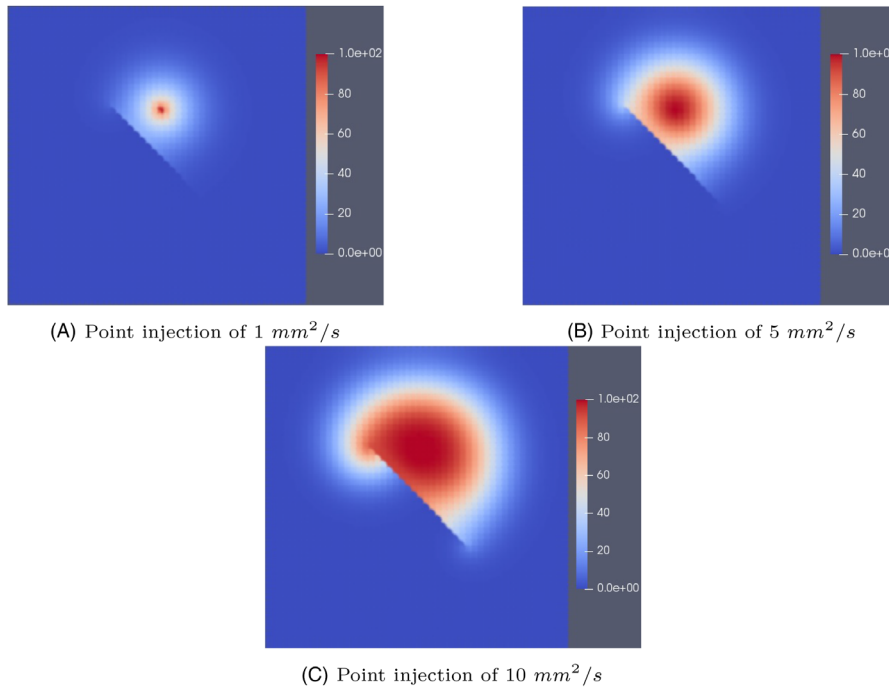
(A) Point injection of 1 mm^2/s

(B) Point injection of 5 mm^2/s

(C) Point injection of 10 mm^2/s

FIGURE 13 Temperature profile (^oC) after 1 day of hot water injection.

(A) Before starting the point injection

(B) After point injection of 1 mm^2/s

(C) After point injection of 5 mm^2/s

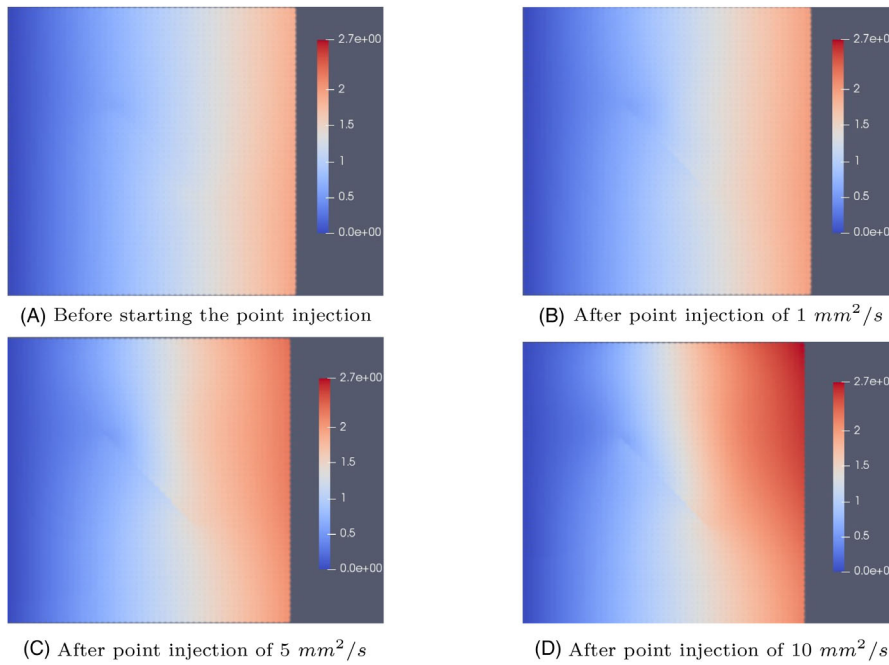(D) After point injection of 10 mm^2/s

FIGURE 14 x-displacement (u_x in mm) contours before and after 1 day of point injection.

With consideration of the cohesive traction contribution in the weak form of the governing equations (30), the variational form of the energy equation may be written as

$$\int_\Omega \boldsymbol{\sigma} : \delta\boldsymbol{\varepsilon}\, d\Omega + \int_\Omega \rho_{av}\ddot{\boldsymbol{u}} \cdot \delta\boldsymbol{u}\, d\Omega - \int_{\Gamma_t} \bar{\boldsymbol{t}} \cdot \delta\boldsymbol{u}\, d\Gamma - \int_\Omega \rho_{av}\boldsymbol{b} \cdot \delta\boldsymbol{u}\, d\Omega - \int_{\Gamma_d} \bar{\lambda}_N \delta g_N\, d\Gamma$$

$$- \int_{\Gamma_d} \bar{\lambda}_T \delta g_T\, d\Gamma + \int_{\Gamma_{coh}} \bar{\boldsymbol{t}}_{\boldsymbol{coh}} \cdot \delta[[\boldsymbol{u}]]\, d\Gamma = 0 \qquad (47)$$

where Γ_{coh} denotes the cohesive zone at the crack tip region.

(A) $t = 2 \times 10^{-4} s$

(B) $t = 4 \times 10^{-4} s$

(C) $t = 6 \times 10^{-4} s$
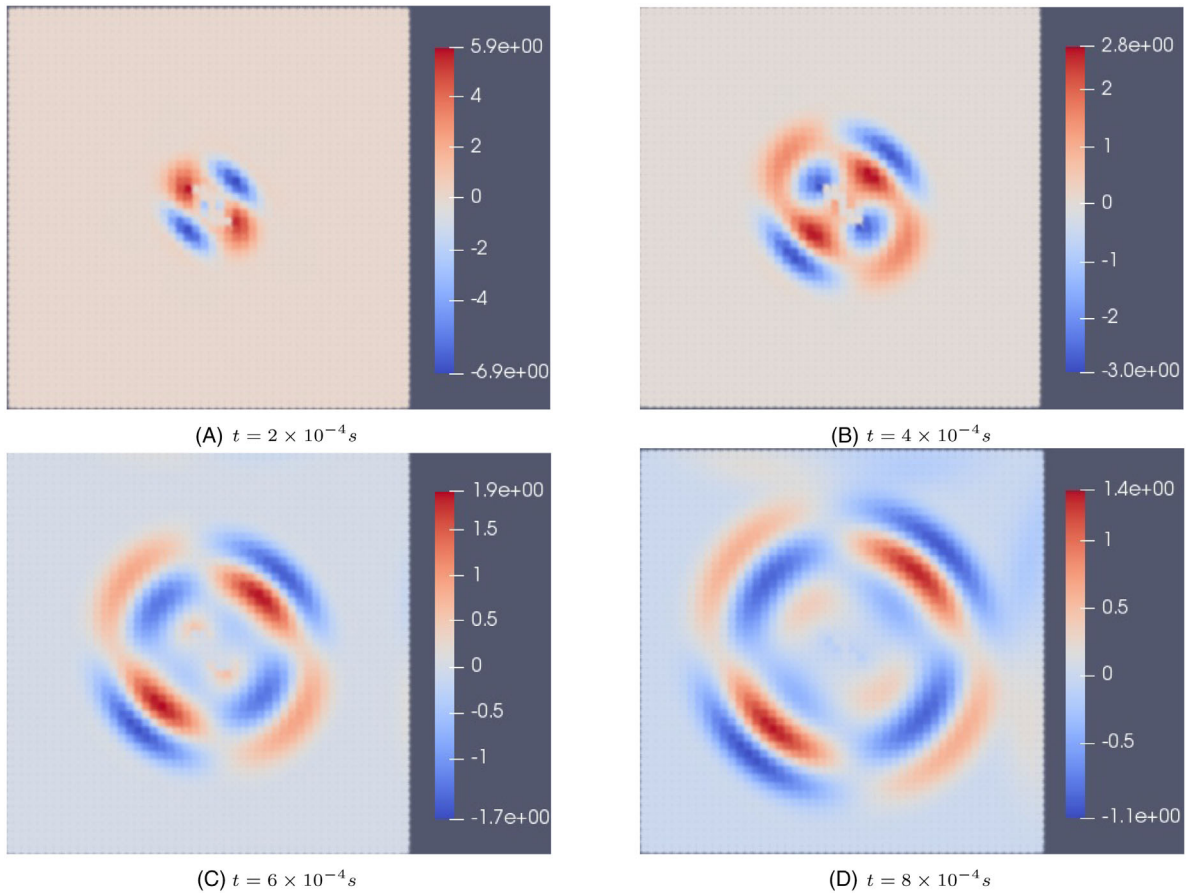
(D) $t = 8 \times 10^{-4} s$

FIGURE 15 Shear wave propagation (rate of x–y rotation) of shear-slip instability-induced microseismic emission.

In the PNM framework, the normal component of the crack opening is denoted as

$$[[u]]_n = \boldsymbol{u}^1 \cdot \boldsymbol{n}^2 + \boldsymbol{u}^2 \cdot \boldsymbol{n}^1 \tag{48}$$

in which the superscripts 1 and 2 are used to indicate the displacement ($\boldsymbol{u}$) as well as the normal unit vector ($\boldsymbol{n}$) to the interface corresponding to the superimposed elements 1 and 2, respectively.

Substituting for the cohesive traction and the separation in Equation (47) using Equations (44) and (48), and with consideration of the GFEM interpolation functions for the displacement fields (33), the contributions of the cohesive tractions (which are modelled as external tractions imposed on internal surfaces) in the force vectors of the finite element equations (34) may be represented as

$$(\boldsymbol{F}_I^{e1})_{coh} = \int_{S_e^{coh}} (\boldsymbol{\psi}_I^1)^\top \left[\sigma_u - \frac{\sigma_u}{\delta_u} \left((\boldsymbol{\psi}_J^1 \boldsymbol{u}_{Jx}^{e1} n_x^{e2}) + (\boldsymbol{\psi}_J^2 \boldsymbol{u}_{Jy}^{e1} n_y^{e2}) \right. \right.$$
$$\left. \left. + (\boldsymbol{\psi}_J^1 \boldsymbol{u}_{Jx}^{e2} n_x^{e1}) + (\boldsymbol{\psi}_J^2 \boldsymbol{u}_{Jy}^{e2} n_y^{e1}) \right) \right] n_x^e d\Gamma_d \tag{49}$$

$$+ (\boldsymbol{F}_I^{e2})_{coh} = \int_{S_e^{coh}} (\boldsymbol{\psi}_I^2)^\top \left[\sigma_u - \frac{\sigma_u}{\delta_u} \left((\boldsymbol{\psi}_J^1 \boldsymbol{u}_{Jx}^{e1} n_x^{e2}) + (\boldsymbol{\psi}_J^2 \boldsymbol{u}_{Jy}^{e1} n_y^{e2}) \right. \right.$$
$$\left. \left. + (\boldsymbol{\psi}_J^1 \boldsymbol{u}_{Jx}^{e2} n_x^{e1}) + (\boldsymbol{\psi}_J^2 \boldsymbol{u}_{Jy}^{e2} n_y^{e1}) \right) \right] n_y^e d\Gamma_d \tag{50}$$

where n_x^e and n_y^e are the x and y components of the unit normal vectors at the interface, respectively, and the superscripts e refer to the superimposed elements ($e = 1$ or 2). Superscripts $e1$ and $e2$ denote the corresponding
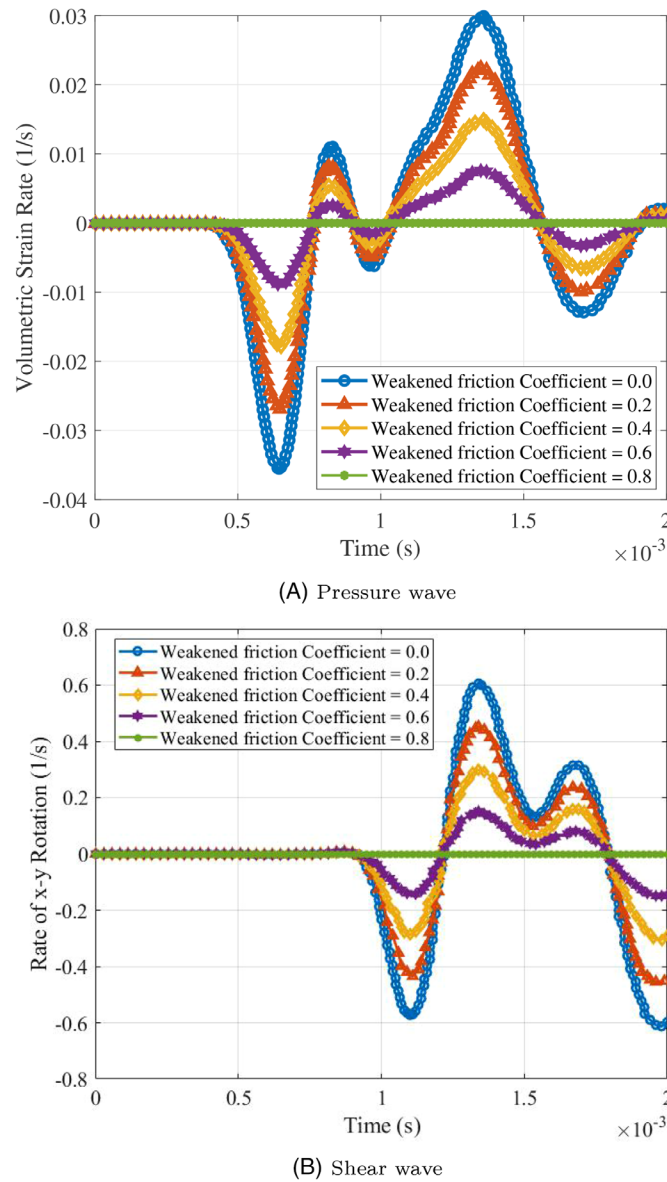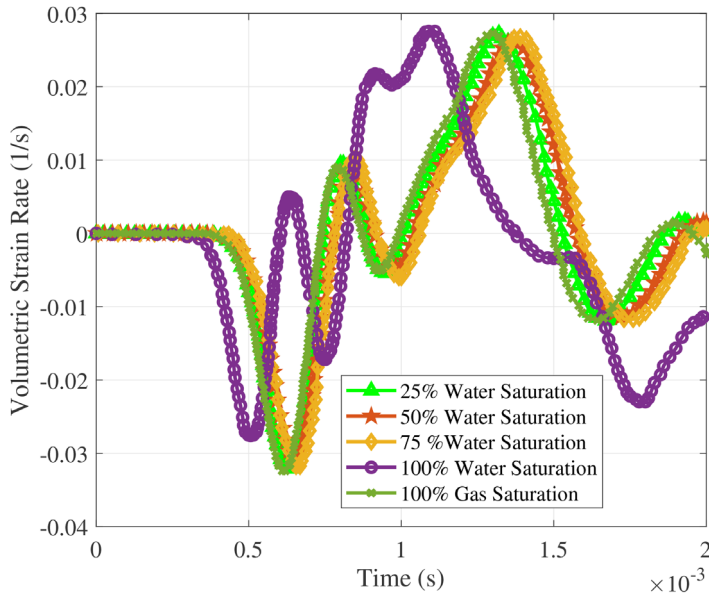
FIGURE 16 Microseismic emission induced by shear-slip instability for various values of the weakened inter-facial friction (the initial friction coefficient $\mu_f = 0.8$).
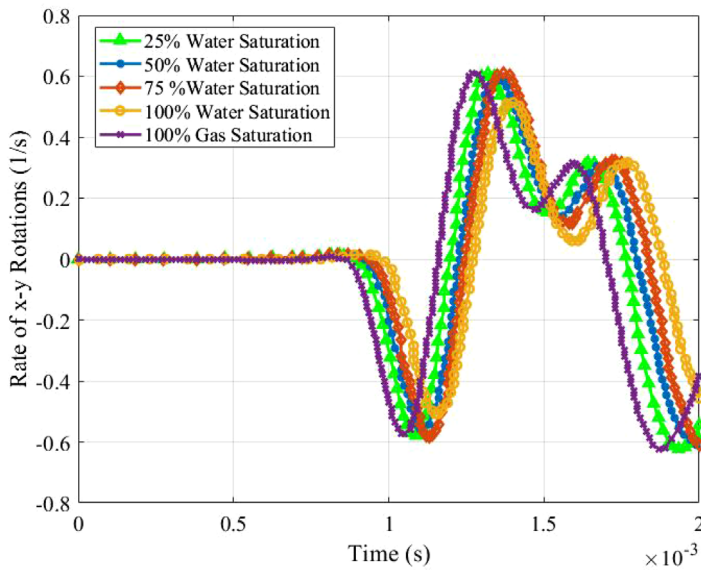
components associated with the superimposed elements 1 and 2, respectively. For more detailed representation of the enriched finite element formulation for the cohesive fracture contribution, one may see Komijani et al.[27]

Do determine the onset of fracture propagation, the maximum tensile principle stress is monitored at all the integration points in the element ahead of the current fracture tip. When the maximum tensile stress at an integration point reaches the ultimate tensile strength of the material, fracture is extended into the element. The direction of fracture extension is calculated using the so-called non-local stress tensor (see Mergheim et al.[45]) which is used at the fracture tip to obtain the direction of the averaged maximum principle stress. The discontinuity is propagated in the direction perpendicular to the non-local maximum principal stress.

In the present discontinuity and fracture propagation modelling, no internal pressure is considered to be exerted on fracture faces, and the crack surfaces are assumed impervious (i.e. strong pore pressure discontinuity across the fracture interface). In other words, there is no hydraulic connection across the fracture and between the pore fluids of the surrounding porous medium and the fluid inside the crack's aperture.

FIGURE 17 Microseismic emission signals at $(x = y = 443.87mm)$ location in the case of $k = 0.29 \times 10^{-13} \, m^2$ permeability, for various pore fluid saturations.

5 | RESULTS AND DISCUSSION

5.1 | Verification studies

To the best of the authors' knowledge, there is no work reported in the literature on explicit simulation of the coupled phenomenon of localization and induced acoustic and ME in multi-phase porous media. To evaluate the robustness and accuracy of the developed computational model, the numerical results are compared with some available data in the literature.

5.1.1 | Consolidation of a soil column

As a first example, the consolidation of a porous vertical column containing water–gas mixture is considered as illustrated in Figure 2. The domain is discretized using 100 rectangular structured bilinear elements across the longitudinal direction
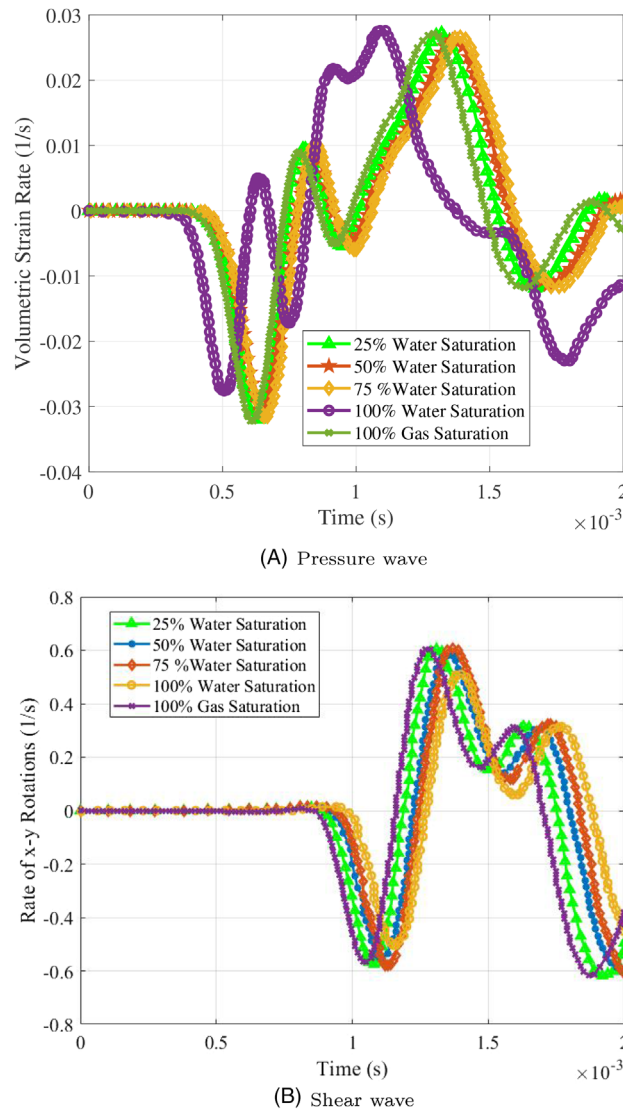
FIGURE 18 Microseismic emission signals at $(x = y = 443.87mm)$ location in the case of $k = 0.29 \times 10^{-12} \, m^2$ permeability, for various pore fluid saturations.

of the column. The material properties of solid and fluid constituents are provided in Table 1. A material interface is considered in the column located at 0.51 m from the bottom. The Young's modulus is considered to be discontinuous across the interface (Young's modulus is set to 6 MPa above the interface and 3 MPa below the interface). The normal displacements at the lateral surfaces as well as at the bottom edge are restricted through boundary conditions while being hydraulically impervious. The initial water saturation in the domain is assumed to be $S_w = 0.52$ and the gas is considered to be exposed to the atmospheric pressure. An external compressive traction of 1000 Pa is exerted at the top surface of the column. The pore water pressure at the top surface is changed abruptly from -280 to -420 KPa, while the gas phase at the top surface remains exposed to the atmospheric pressure. The constitutive saturation-capillary pressure relations as well as the relative permeabilities are assumed according to the relations proposed by Brooks and Corey.[43] This yields the residual (irreversible) water saturation $S_{rw} = 0.3966$, the gas–water displacement pressure $p_{dgw} = 225$ kN/m^2, the pore size distribution index $\lambda = 3$. Furthermore, the residual saturation of the gas phase (a non-wetting phase) is set to zero (see Equations 16 and 19).

Figure 3 depict variations of saturation and capillary pressure through the height of the column at different times in the consolidation process. The results obtained, using the non-linear model developed in this work, are compared with those previously reported in Refs. 40, 46 with observation of very close agreements.
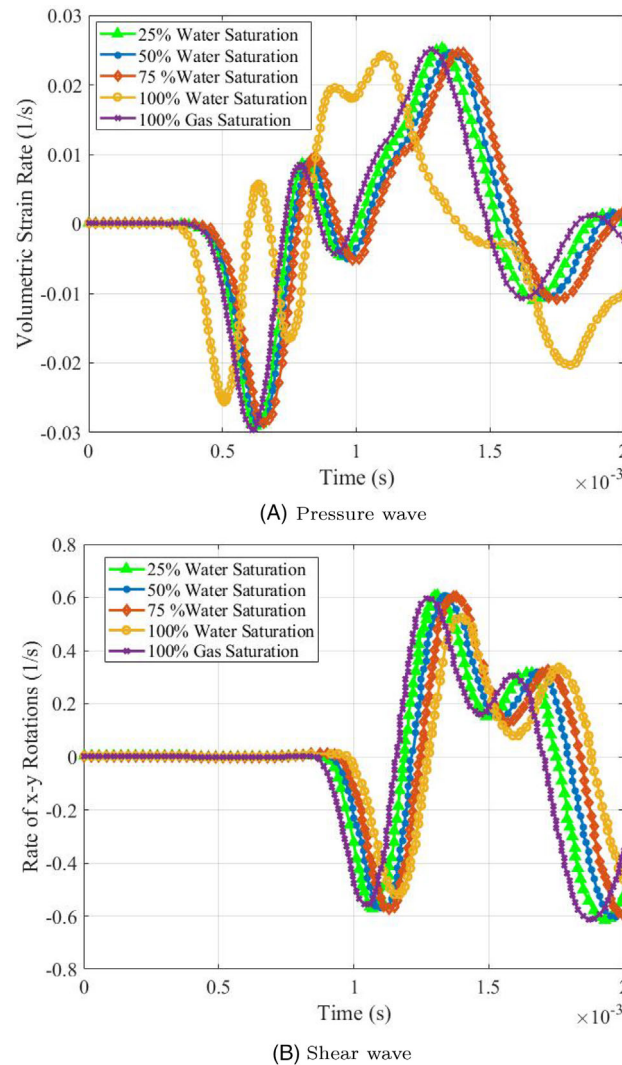
FIGURE 19 Microseismic emission signals at $(x = y = 443.87mm)$ location in the case of $k = 0.29 \times 10^{-11}\ m^2$ permeability, for various pore fluid saturations.

5.1.2 | Thermo-hydro-mechanical simulation of a two-dimensional porous medium with an inclined fault

To test the computational accuracy of the developed non-linear THM model, a two-dimensional porous medium with an inclined adiabatic and impervious fault/discontinuity (with inclination angle β) in the middle is considered as illustrated schematically in Figure 4. The material properties of the solid and fluid phases are listed in Table 2. The bottom surface is exposed to water flux injection at constant temperature of $(T = 100\ °C)$ while the top surface is permeable at pressure $(p = 0)$ and temperature $(T = 0\ °C)$. The other lateral surfaces are kept impervious. A 20 by 20 structured rectangular element mesh is used for the simulations.

The graphs in Figure 5 show water pressure time histories at points $B\ (x = 5.13m, y = 4.87m)$ for the case of intact domain and faulted domain with different inclination angles of the discontinuity. The results obtained herein are in very close agreement with those reported in Khoei and Saeedmonir.[40]

Temperature profiles along y-axis at the middle of the domain (i.e. through the line $x = 5m$) are depicted in Figure 6 for different times of the simulation with consideration of diffusive and advective–diffusive (convective) heat transfer natures in the case of inclination angle $\beta = 45°$. As observed, in the steady-state condition of heat transfer (Figure 6C), the developed temperature profile for the case of diffusive/conduction heat transfer (linear problem with neglecting fluid flow (mass transfer) coupling in thermal problem) has a uniform slope, consistent with the Fourier's heat conduction law.
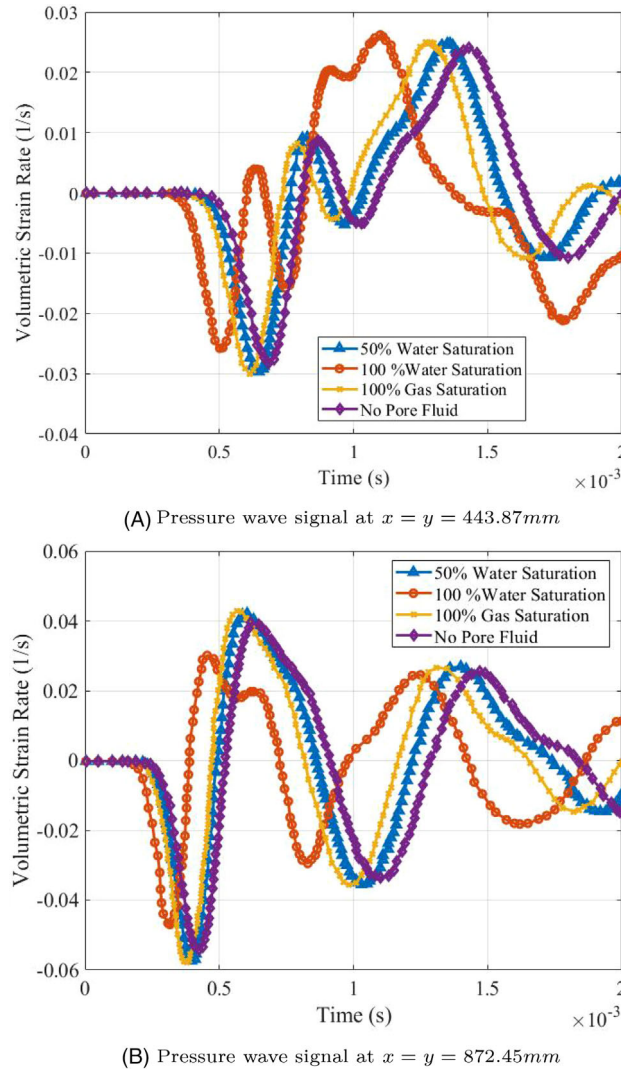
(A) Pressure wave signal at $x = y = 443.87mm$

(B) Pressure wave signal at $x = y = 872.45mm$

FIGURE 20 Pressure wave signals at two locations in the case of $k = 0.29 \times 10^{-13} \; m^2$ permeability, for various pore fluid saturations.

On the other hand, in the case of advective–diffusive (convection) heat transfer (non-linear problem with accounting for the effect of fluid flow (mass transfer) coupling in thermal problem), the corresponding slope of the temperature profile is quite non-uniform and the steady-state condition is reached when the temperature in the interior of the domain becomes equal to the temperature of the injecting hot water. It is noted that the jump observed in the temperature profiles at the middle of the curves are due to the pre-existing adiabatic fault in the domain. The graphs in Figure 7 demonstrate water pressure variations along *y*-axis at the middle of the domain for different cases of intact and fractured media. The noticed jump in the pressure profiles of the fractured cases are due to the impervious condition considered across the fault interface.

5.2 | Coupled thermo-hydro-mechanical modelling in a soil column

To demonstrate the computational capability and robustness of the developed FE model in simulations regarding the multi-physics response of porous media with multi-phase fluid flow and thermal coupling, the soil column studied in Section 5.1.1 using the same materials, geometry and boundary conditions is considered. The top surface is exposed suddenly to hot water injection at constant pressure of $-140kPa$ with 100 ^oC temperature. One hundred rectangular elements are considered in the height direction of the column for the numerical solution. Figure 8 shows the evolution process of diffusive heat transfer into the soil column. As observed, a thermal equilibrium is attained eventually at uniform
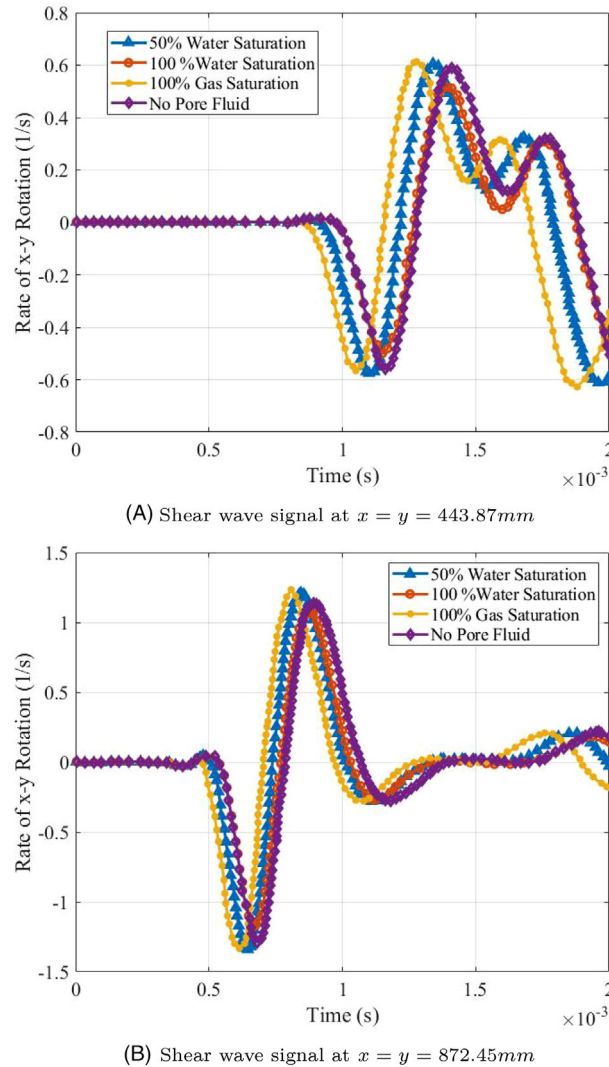
(A) Shear wave signal at $x = y = 443.87mm$

(B) Shear wave signal at $x = y = 872.45mm$

FIGURE 21 Shear wave signals at two locations in the case of $k = 0.29 \times 10^{-13}\ m^2$ permeability, for various pore fluid saturations.

temperature distribution of $100\ ^oC$ which is physically foreseeable. Variations of water and gas saturations and pressures in the height of the column are presented in Figure 9 at different times after the water injection starts at the top surface. The diffusive process of water pressure increase and gas discharge from the top surface is well illustrated in the plots.

5.3 │ Simulation of stick–slip behaviour at a pre-existing crack interface

Simulation of stick–slip frictional contact behaviour at a discrete crack interface is of importance in geo-containment and integrity of subsurface engineering operations, particularly in induced fault reactivation and seismicity. To demonstrate the robustness of the developed numerical model in simulation of interface stick-slip behaviour under THM loads, a two-dimensional porous domain with two-phase fluid of 50% water and 50% air saturation (air/gas phase at initial pressure of $p_g = 0MPa$) with a discrete crack of length $1.41m$ placed at 45ž angle with horizontal direction (see Figure 10) is considered. The domain is subject to a vertical overburden stress of $10MPa$ imposed on the top surface. The material properties used in the simulation are given in Table 3. A 49 by 49 structured rectangular finite element mesh is considered for the simulation. Figure 11 illustrates x-displacement contours of the fractured medium for various friction coefficients at the interface of fracture. By increasing the friction coefficient (μ_f), transition from slip to stick–slip and full stick behaviour is observed at the interface.
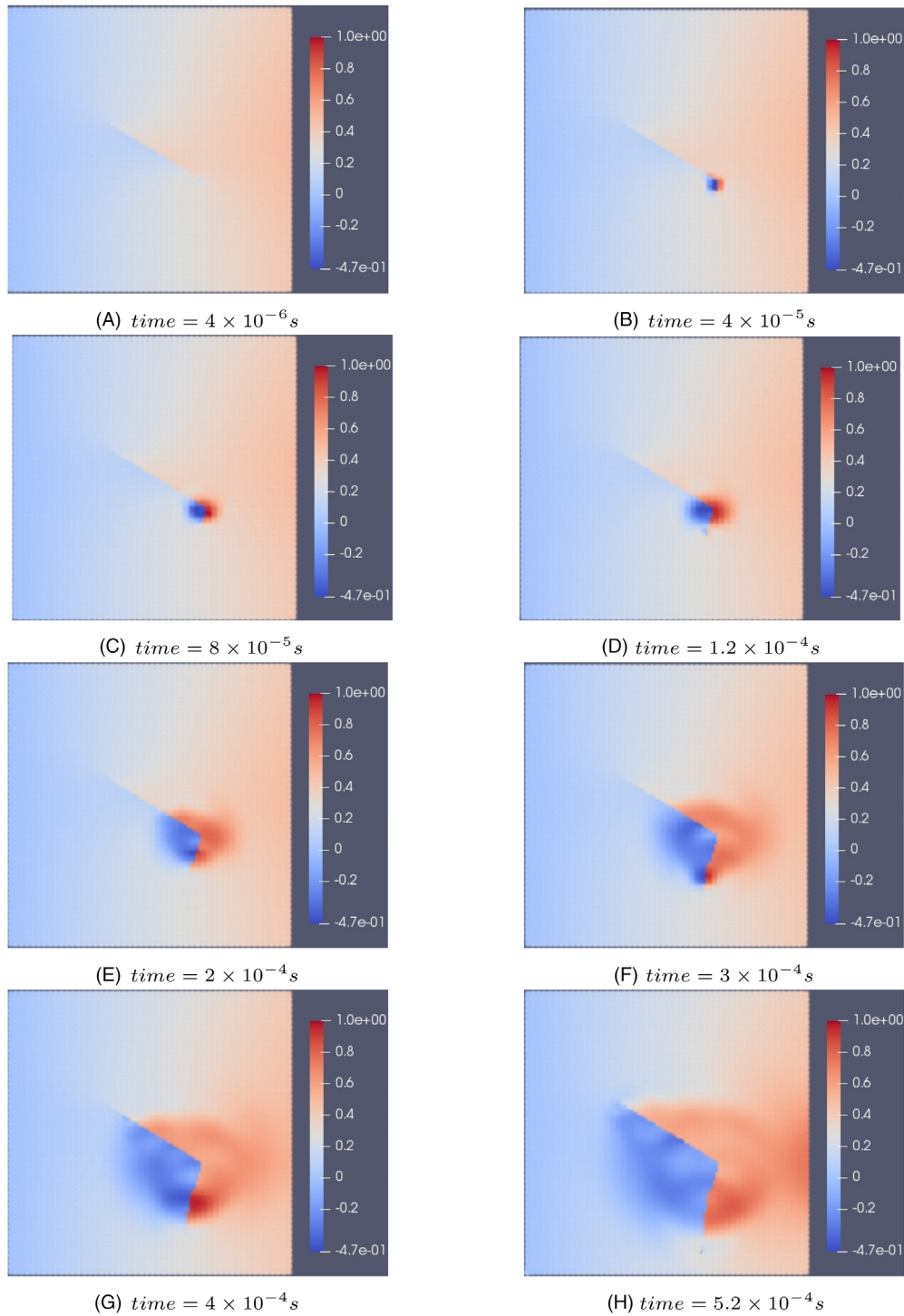
(A) $time = 4 \times 10^{-6} s$

(B) $time = 4 \times 10^{-5} s$

(C) $time = 8 \times 10^{-5} s$

(D) $time = 1.2 \times 10^{-4} s$

(E) $time = 2 \times 10^{-4} s$

(F) $time = 3 \times 10^{-4} s$

(G) $time = 4 \times 10^{-4} s$

(H) $time = 5.2 \times 10^{-4} s$

FIGURE 22 x-displacement (u_x in mm) contours in different crack propagation steps.

To more clearly illustrate the localized shear slip orientation along the discontinuity interface, Figure 12 presents vector plots of the displacement field **u** for $\mu_f = 0.05$ (slip condition) and $\mu_f = 1$ (stick condition).

To simulate reactivation of pre-existing fracture under hydro-thermal loading, the porous medium schematically shown in Figure 10 is considered again. The domain is initially under in situ stress condition due to a vertical confining stress as shown. To demonstrate the effect of the thermal coupling in induced pre-existing fracture reactivation, a point injection of hot water with ($T = 100^o C$) imposed at ($x = 1.53m, y = 1.96m$) location is applied as an stimulation source. The friction coefficient at the interface is assumed to be $\mu_f = 1$. Temperature profiles after 1 day of injection are plotted in Figure 13
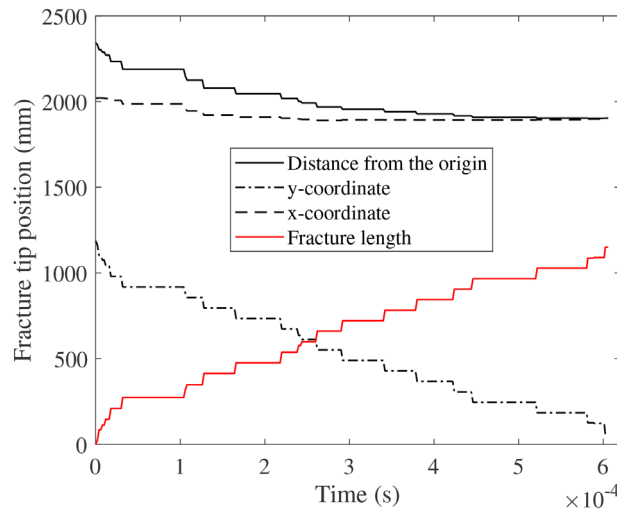
FIGURE 23 Time history of the fracture tip position and fracture length in the fracture propagation process. The origin of the coordinate system is considered to be at the bottom left corner.

for different injection rates. As seen, the evolution of temperature in the advective–diffusive (i.e. convective) heat transfer process depends on the injection rate. For a higher injection rate, the temperature profile evolves faster into the formation showing the effect of thermal coupling in the model which results in shear slip (reactivation) at the interface due to the induced thermal and hydraulic stresses/deformations. Figure 14 shows x-displacement (u_x in mm) contours before injection and after 1 day of injection with different injection rates. Reactivation of the pre-existing fracture and the direct proportionality of the induced shear slip at the interface with hot water injection rate is well observed in the figures.

5.4 | Simulation of microseismic emission induced by shear-slip instability at a pre-existing crack

ME induced by shear-slip instability at a pre-existing crack is modelled in this section for the case of a $3m$ by $3m$ rectangular porous medium with an inclined crack of length $0.28m$ located at the middle of the domain and at 135° with respect to the horizontal direction. The origin of the xy coordinate system is considered at the bottom left corner of the physical domain. The boundary and external loading (vertical confining stress) conditions are the same as in the case shown in Figure 10. A 49 by 49 rectangular structured finite element mesh is considered for the numerical model. The friction coefficient at the interfaces of the pre-existing sloping crack is $\mu_f = 0.8$. The material properties used for the simulation are listed in Table 3. The initial saturations of the fluid phases are considered to be 50% water and 50% air (air/gas phase at initial pressure of $p_g = 0MPa$). The rate of the x–y rotation and the volumetric strain rate are considered as the wave function for demonstration of the shear (S) and the pressure (P) waves, respectively. In the remaining parts of this paper where the results for induced acoustic and MEs are discussed, the S wave function is twice the rate of the x–y component of the rotation tensor ($\omega_{xy} = \frac{1}{2}(u_{x,y} - u_{y,x})$). The rotation tensor is the antisymmetric part of the deformation gradient. Also, the P wave function is considered to be the rate of the divergence of the displacement field ($\dot{\varepsilon}_v = \dot{u}_{x,x} + \dot{u}_{y,y}$), which is the rate of the volumetric strain. A proportional damping in the form of $\mu_1[M] + \mu_2[K]$ ([M] and [K] being the inertia and stiffness components of the solid phase) is assumed to account for the physical damping/material attenuation in the solid skeleton. μ_1 and μ_2 are the damping coefficients associated with the mass and stiffness matrices of the solid phase, respectively. In the following wave propagation numerical results, the damping coefficients are assumed to be $\mu_1 = \mu_2 = 10^{-5}$.

To mimic a seismic slip behaviour caused by slip-weakening phenomenon at interface, a sudden release of frictional forces at the discontinuity is modelled through changing the friction coefficient from the initial value of $\mu_f = 0.8$ to $\mu_f = 0.0$. Figure 15 exhibits the S wave propagation pattern of the induced ME at different time steps following the onset of the shear-slip instability. To study the effect of the interface weakening on the intensity of the induced ME, Figure 16 depicts S and P wave signals recorded at point ($x = y = 443.87mm$) for different magnitudes of the weakened friction coefficient. As observed, there is a direct relation between the amount of the interface weakening and the magnitude of the emitted wave signals for both the pressure and shear wave types. However, the frequency of the signals appears to be
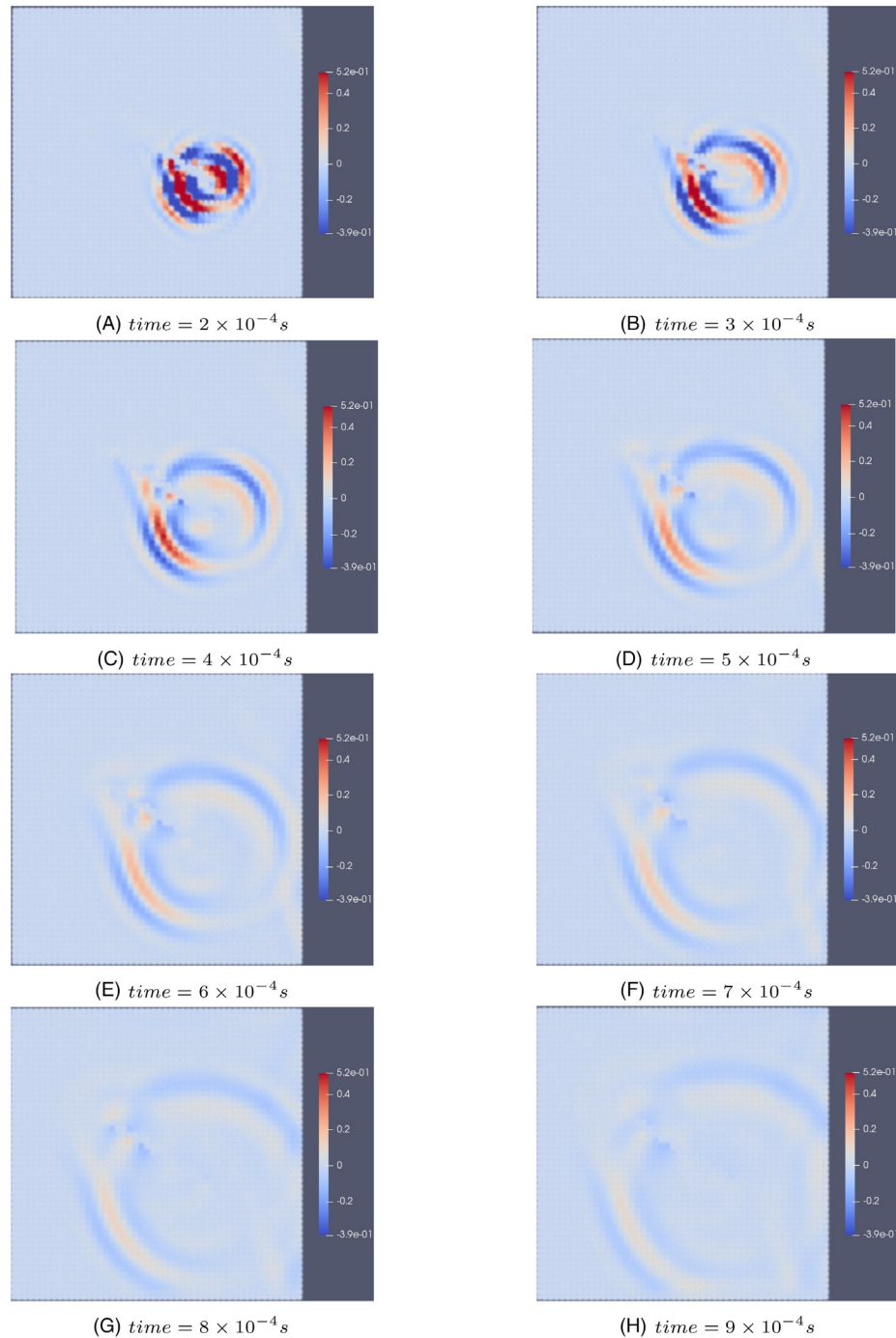
(A) $time = 2 \times 10^{-4} s$

(B) $time = 3 \times 10^{-4} s$

(C) $time = 4 \times 10^{-4} s$

(D) $time = 5 \times 10^{-4} s$

(E) $time = 6 \times 10^{-4} s$

(F) $time = 7 \times 10^{-4} s$

(G) $time = 8 \times 10^{-4} s$

(H) $time = 9 \times 10^{-4} s$

FIGURE 24 Shear (S) wave propagation induced by tensile fracturing; x–y rotation rate ($2\,\dot{\omega}_{xy}$) contours at different time steps.

almost independent of the interface weakening. The higher speed of the P wave in comparison with the S wave is also clear in the plots ($V_P \approx 3734\ m/s$ and $V_S \approx 1659\ m/s$).

Figures 17–19 illustrate the effect of fluid phases (water and gas) saturations on induced microseismic signals at ($x = y = 443.87mm$) location for permeability magnitudes of $k = 0.29 \times 10^{-13}\ m^2$, $k = 0.29 \times 10^{-12}\ m^2$ and $k = 0.29 \times 10^{-11}\ m^2$, respectively. The wave emissions are induced by abruptly changing the interface friction coefficient from the initial value of $\mu_f = 0.8$ to $\mu_f = 0.0$. Based on the exhibited numerical results, the velocity of the P and S waves are dependent on the degree of saturation of the fluid phases. In all of the examined permeability cases, the P wave velocity in porous medium fully saturated with water ($S_W = 100\%$, $S_g = 0\%$) appears to be higher than other combinations of water and gas saturation. On the other hand, the S wave velocity in medium fully saturated with water seems to be the lowest.

For the S wave signals, the cases with full gas saturation ($S_W = 0\%$, $S_g = 100\%$) are shown to have the highest speed of the shear wave.

#nag3608-fig-0017.fig #nag3608-fig-0018.fig #nag3608-fig-0019.fig In Figures 20 and 21, the recorded signals for the case with $\boldsymbol{k} = 0.29 \times 10^{-13} \; m^2$ permeability are depicted at locations ($x = y = 443.87mm$) and ($x = y = 872.45mm$) for P and S wave components, respectively. It can be noticed that the induced waves have their lowest velocities in cases with no pore fluid (purely elastic media), and the existence of the pore fluid constituents (porous media) contributes to the velocities of the induced waves (in both pressure and shear waves). For the case of ($S_W = 100\%$, $S_g = 0\%$), the approximate average estimated P wave velocity at $x = y = 443.87mm$ is $V_P \approx 4667.5 \; m/s$, while being $V_P \approx 5916.6 \; m/s$ at $x = y = 872.45mm$, which shows a decreasing trend for the velocity of the pressure wave as the wave propagates farther. For the S wave case, at $x = y = 443.87mm$, the velocity $V_S \approx 1572.2 \; m/s$ and at $x = y = 872.45mm$, the velocity $V_S \approx 1775 \; m/s$. Similar comparison between the velocities of the shear waves at the two locations shows that the shear wave velocity also tends to diminish as the wave propagates through the medium. However, the rate of the velocity reduction of the pressure wave is apparently much faster than the reduction rate of the shear wave velocity.

5.5 | Simulation of discrete fracture propagation

To demonstrate the robustness and versatility of the developed numerical model in simulating discrete fracture propagation, an axial splitting problem with fracture extension under compression is solved. The geometry of the problem is the same as the one schematically shown in Figure 10, with pre-existing sloping crack of length $1.16m$ being at angle of 149ž to the horizontal direction. The friction coefficient at the crack interface is $\mu_f = 0.05$. The material properties are given in Table 3 with considering the fracture energy to be $G_F = 100N/mm$ and the tensile strength of solid material as $\sigma_{ult} = 1MPa$. The initial water and gas saturations are considered to be $S_w = 80\%$ and $S_g = 20\%$ with in situ gas pressure of $p_g = 0 \; MPa$. A 49 by 49 structured rectangular finite element mesh is considered for the simulation. A compressive external traction of the following form is imposed at the top surface to induce fracture propagation under compression:

$$\bar{t}(t) = \begin{cases} 10 \; sin\left(\dfrac{\pi}{2\hat{t}}t\right) \; [MPa] & \text{if } t \leqslant \hat{t}; \\ 10 & \text{if } t > \hat{t}. \end{cases} \tag{51}$$

In this simulation, to avoid stimulation of inertia effects in the primary loading process, the damping coefficients are assumed to be $\mu_1 = \mu_2 = 1$ and $\hat{t} = 800s$. Fracture propagation starts at $t = 128.0498s$ (i.e. $\bar{t} = 2.4878 \; MPa$). At the onset of fracture instability, the damping coefficients are changed to $\mu_1 = \mu_2 = 0.00001$ in order to include the inertia effects in the dynamic process of fracture propagation. Figure 22 demonstrates x-displacement contours and the fracture path and evolution process at different time steps following the propagation of the pre-existing crack. Figure 23 is plot of the fracture tip location as a function of time following the instability/activation of the right tip of the pre-existing crack. The variation of fracture length with time is also depicted in Figure 23 which conventionally is considered a more valuable information to provide. The time-axis illustrates the time starting from the onset of propagation.

5.6 | Simulation of acoustic emission induced by tensile fracture propagation

Simulation of AE induced by tensile fracture propagation is carried out for the fractured porous medium discussed in Section 5.5 with consideration of the same finite element mesh. Fracture energy is considered to be $G_F = 0.1N/mm$. Figure 24 exhibits AE propagation pattern for the shear wave induced by one segment of fracture extension. The wave propagation phenomenon is illustrated by snapshots at different time steps (each time step is $\Delta t = 2 \times 10^{-6}s$). The wave function considered to show the propagation of the induced shear wave phenomenon is twice the rate of the x–y component of the rotation tensor. The rotation tensor is the antisymmetric part of the deformation gradient ($\omega_{xy} = \frac{1}{2}(u_{x,y} - u_{y,x})$).

Figure 25 demonstrates time histories of pressure (P) and shear (S) waves at point ($x = 994.89mm$ and $y = 811.22mm$) for different water and gas saturation values. As observed, the degree of saturation of fluid phases has noticeable effect on induced AE signals and the velocity of P and S waves.
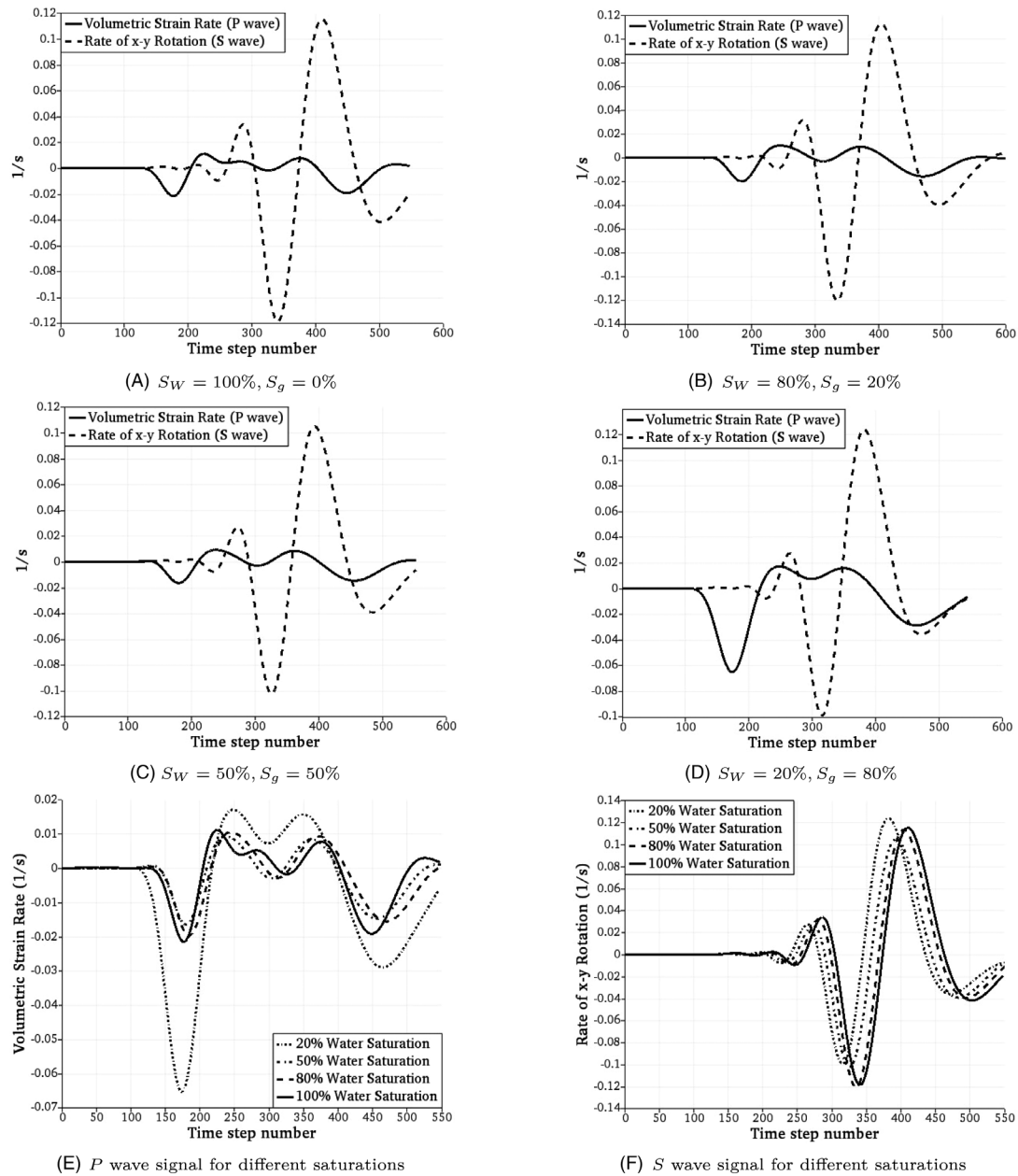
(A) $S_W = 100\%$, $S_g = 0\%$

(B) $S_W = 80\%$, $S_g = 20\%$

(C) $S_W = 50\%$, $S_g = 50\%$

(D) $S_W = 20\%$, $S_g = 80\%$

(E) P wave signal for different saturations

(F) S wave signal for different saturations

FIGURE 25 P and S wave signals at point $x = 994.89mm$ and $y = 811.22mm$ for different degrees of saturation. Each time step on the horizontal-axis represents $\Delta t = 2 \times 10^{-6}s$ starting from the onset of fracture propagation.

Figure 26 shows effect of the fracture energy (G_F) on the induced AE signals at point ($x = 474.5mm$ and $y = 382.6mm$) for the case of $S_W = 80\%$, $S_g = 20\%$. As can be seen, the smaller the fracture energy, the more pronounced the AE signal is for P wave. On the other hand, the fracture energy appears to have very minimal effect on the induced signal for the S wave. The more pronounced pressure wave signal observed for lower fracture energy magnitudes is because of the more brittleness of the material and therefore, less energy dissipates in the fracturing and stress degradation process.

6 | CONCLUSIONS

A novel mixed finite element formulation is proposed for simulation of AE and ME induced by discrete fracture propagation and shear-slip instability/localization at pre-existing interfaces. Porous media with multi-phase fluid flow and thermal coupling is considered as the domain of analysis. The coupled non-linear system of equations is developed based on the generalized Biot's mixture theory.
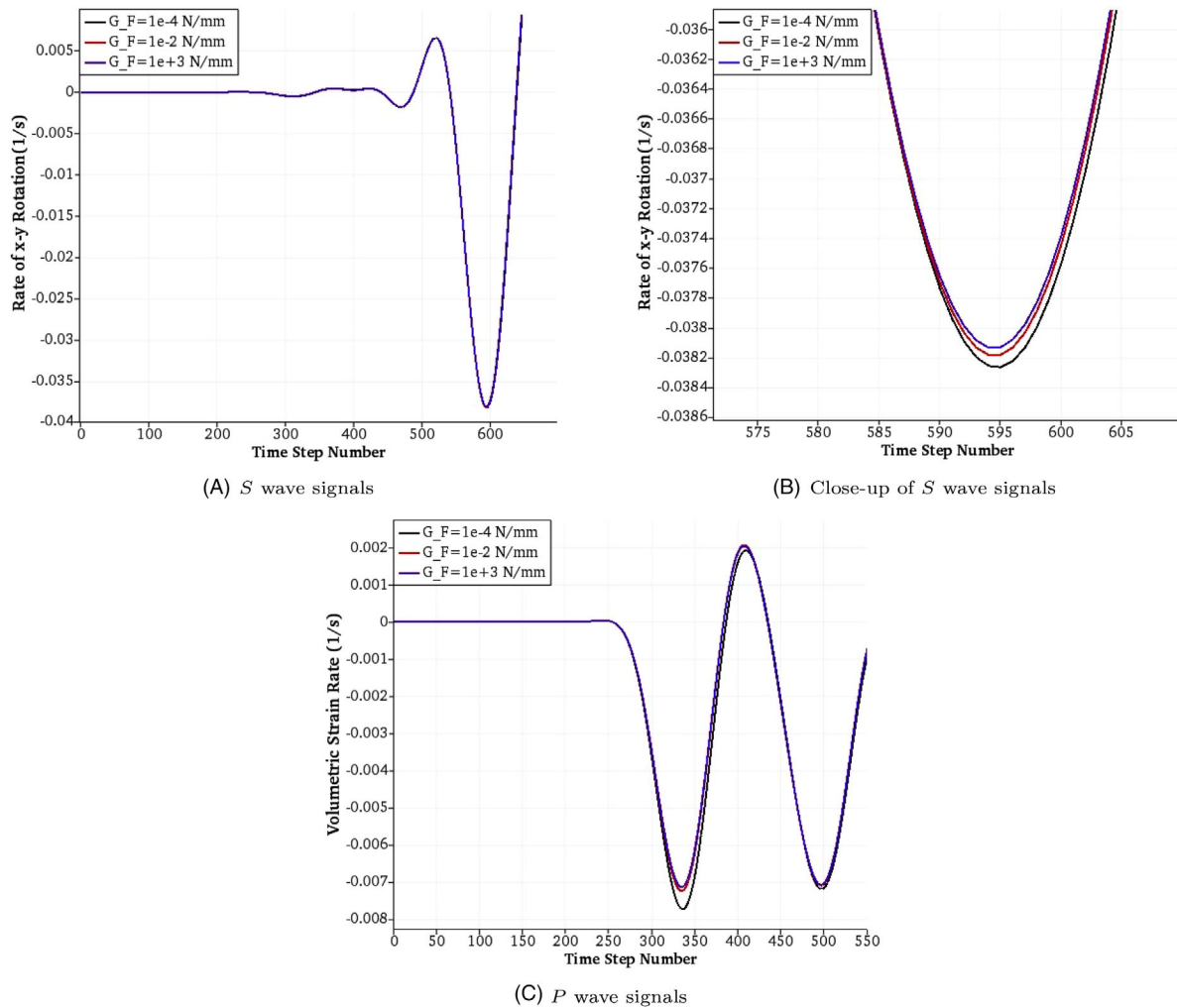
(A) S wave signals

(B) Close-up of S wave signals

(C) P wave signals

FIGURE 26 Effect of the fracture energy (G_F) on induced AE P and S wave signals.

The versatility of the PNM in modelling discrete discontinuities is used to simulate pre-existing fractures and fracture propagation independently of the original mesh and with no need for re-meshing. An augmented Lagrange multiplier method is employed to model the stick–slip frictional contact at discrete discontinuities through an iterative manner. The cohesive fracture model is implemented to simulate the tensile stress degradation and localization in the fracture process zone for dynamic crack extension.

The computational capability and robustness of the developed model in simulating the non-linear solid–multi-phase fluid interactions with thermal coupling, stick–slip frictional contact at pre-existing and induced fractures, fracture propagation, and induced acoustic and MEs are demonstrated through various numerical examples. Effects of different system parameters such as, permeability, multi-phase pore fluid saturations and fracture energy on induced acoustic and microseismic signals are investigated.

To the best of the authors' knowledge, there is no available data that can be appropriate and applicable to use for validation study of the present model setups from experiments or analytical solutions in the case of induced acoustic or ME in fractured porous media with multi-phase flow and thermal coupling. This study is mostly concentrated on simulation of localization-induced acoustic and MEs and there has been less emphasize on interface constitutive modelling and details of the localization and degradation at the interface level, particularly in the shear failure mode. There are very limited number of papers available in the literature on simulation of induced acoustic and ME in fractured porous media in the context of the continuum mechanics and elasto-dynamics. The present mathematical, numerical and particularly the interface constitutive models considered in this article need to be further extended and more complexities need to be added to make the model more versatile and reliable for simulation of a variety of real case problems in sub-surface engineering and geomechanics, which usually contain significant complexities and uncertainties. This matter can be

quite important in the accuracy and validity of the simulated induced acoustic and MEs in real case and complex coupled non-linear applications.

Therefore, future research works with focus on rigorous modelling of the physics of softening and damage localization processes in shear and tensile modes would be of great value. Moreover, extension of the existing numerical model to the cases considering coupling between fluid flow inside fractures and the flow in the porous matrix would be of practical value in applications like HF. Last but not least, the existing two-dimensional model may be extended to a more general three-dimensional simulator in future works. Unlike the extension procedure of continuous thermo-poro-elastic models without discrete cracks and fracture propagation, in the context of the XFEM and enriched finite element models for simulation of discrete discontinuities, extension to three-dimensional may not be as straightforward and trivial and requires a great deal of time and effort within a separate scope of research work. Considering the current size and contents of this paper in the mathematical formulation, numerical models and the parametric studies, future results of the axis-symmetric model and the 3D model will be disseminated through separate papers.

DATA AVAILABILITY STATEMENT

Data sharing not applicable to this article as no datasets were generated or analysed during the current study.

ORCID

Mohammad Komijani https://orcid.org/0000-0002-0109-2360

REFERENCES

1. Jha B, Juanes R. A locally conservative finite element framework for the simulation of coupled flow and reservoir geomechanics. *Acta Geotech*. 2007;2(3):139-153.
2. Moeendarbary E, Valon L, Fritzsche M, et al. The cytoplasm of living cells behaves as a poroelastic material. *Nat Mater*. 2013;12(3):253-261.
3. Fraldi M, Carotenuto AR. Cells competition in tumor growth poroelasticity. *J Mech Phys Solids*. 2018;112(3):345-367.
4. Cusini M, White JA, Castelletto N, Settgast RR. Simulation of coupled multiphase flow and geomechanics in porous media with embedded discrete fractures. *Int J Numer Anal Methods Geomech*. 2021;45(5):563-584.
5. Liu F. Modeling fracture propagation in a rock-water-air system with the assumed enhanced strain method. *Int J Numer Methods Eng*. 2022;123(11):2429-2466.
6. Shauer N, Desmond KW, Gordon PA, Liu F, Duarte, CA,. A three-dimensional Generalized Finite Element Method for the simulation of wave propagation in fluid-filled fractures. *Comput Methods Appl Mech Eng*. 2021;386:114136.
7. Khoei AR, Saeedmonir S. Computational homogenization of fully coupled multiphase flow in deformable porous media. *Comput Methods Appl Mech Eng*. 2021;376:113660.
8. Saeedmonir S, Khoei AR. Multiscale modeling of coupled thermo-hydro-mechanical analysis of heterogeneous porous media. *Comput Methods Appl Mech Eng*. 2022;391:114518.
9. Wu Z, Cui W, Weng L, Liu Q. A 2D FDEM-based THM coupling scheme for modeling deformation and fracturing of the rock mass under THM effects. *Comput Geotech*. 2022;152:105019.
10. Faust CR. Transport of immiscible fluids within and below the unsaturated zone: a numerical model. *Water Resour Res*. 1985;21(4):587-596.
11. Faust CR, Guswa JH, Mercer JW. Simulation of three-dimensional flow of immiscible fluids within and below the unsaturated zone. *Water Resour Res*. 1989;25(12):2449-2464.
12. Panday S, Wu YS, Huyakorn PS, Springer EP. A three-dimensional multiphase flow model for assessing NAPL contamination in porous and fractured media, 2. Porous medium simulation examples. *J Contam Hydrol*. 1994;16:131-156.
13. Cao TD, Hussain F, Schrefler BA. Porous media fracturing dynamics: stepwise crack advancement and fluid pressure oscillations. *J Mech Phys Solids*. 2018;111:113-133.
14. Rethore J, De Borst R, Abella MA. A discrete model for the dynamic propagation of shear bands in a fluid-saturated medium. *Int J Numer Anal Methods Geomech*. 2007;31(2):347-370.
15. Lockner D. The role of acoustic emission in the study of rock fracture. *Int J Rock Mech Min Sci Geomech Abstr*. 1993;30(7):883-899.
16. Carpinteri A, Xu J, Lacidogna G, Manuello A. Reliable onset time determination and source location of acoustic emissions in concrete structures. *Cem Concr Compos*. 2012;34:529-537.
17. Xu J, Fu Z, Han Q, Lacidogna G, Carpinteri A. Micro-cracking monitoring and fracture evaluation for crumb rubber concrete based on acoustic emission techniques. *Struct Health Monit*. 2017:1475921717730538.

18. Invernizzi S, Lacidogna G, Carpinteri A. Numerical models for the assessment of historical masonry structures and materials, monitored by acoustic emission. *Appl Sci*. 2016;6(4):102.

19. Pettitt S, Baker C, Young R, Dahlstrom L-O, Ramqvist G. The assessment of damage around critical engineering structures using induced seismicity and ultrasonic techniques. *Pure Appl Geophys*, 2002;159(1-3):179-195.

20. Smith MB, Montgomery C. *Hydraulic Fracturing*, CRC Press; 2015.

21. Warpinski NR, Mayerhofer M, Agarwal K, Du J,. Hydraulic-fracture geomechanics and microseismic-source mechanisms. *SPE J*. 2013;18(04):766-780.

22. Tang C. Numerical simulation of progressive rock failure and associated seismicity. *Int J Rock Mech Min Sci*. 1997;34(2):249-261.

23. Tang CA, Kaiser PK. Numerical simulation of cumulative damage and seismic energy release during brittle rock failure—part I: fundamentals. *Int J Rock Mech Min Sci*. 1998;35(2):113-121.

24. Komijani M, Gracie R. An enriched finite element model for wave propagation in fractured media. *Finite Elements Anal Design*. 2017;125:14-23.

25. Komijani M, Gracie R. Enriched mixed finite element models for dynamic analysis of continuous and fractured porous media. *Comput Methods Appl Mech Eng*. 2019;343:74-99.

26. Komijani M, Gracie R, Sarvaramini E. Simulation of induced acoustic emission in fractured porous media. *Eng Fract Mech*. 2019;210:113-131.

27. Komijani M, Gracie R, Yuan Y. Simulation of fracture propagation induced acoustic emission in porous media. *Eng Fract Mech*. 2020;229:106950.

28. Terzaghi K. *Theoretical Soil Mechanics*. Wiley, New York; 1943.

29. Biot MA. *Mechanics of Incremental Deformations*. Wiley; 1965.

30. Dugdale DS. Yielding of steel sheets containing slits. *J Mech Phys Solids*. 1960;8:100-108.

31. Barenblatt GI. The formation of equilibrium cracks during brittle fracture: general ideas and hypotheses. Axially-symmetric cracks. *J Appl Math Mech*. 1959;23:622-636.

32. Moes N, Belytschko T. Extended finite element method for cohesive crack growth. *Eng Fract Mech*. 2002;69:813-833.

33. Carpinteri A. Notch sensitivity in fracture testing of aggregative materials. *Eng Fract Mech*. 1982;16:467-81.

34. Bazant ZP, Planas J. *Fracture and Size Effect in Concrete and Other Quasi-brittle Materials*. CRC Press; 1998.

35. Song J-H, Areias PMA, Belytschko T. A method for dynamic crack and shear band propagation with phantom nodes. *Int J Numer Methods Eng*. 2006;67:868-893.

36. Zienkiewicz OC, Chan AHC, Pastor M, et al. *Computational Geomechanics with Special Reference to Earthquake Engineering*. John Wiley & Sons, Inc; 1999.

37. Ji H, Dolbow JE. On strategies for enforcing interfacial constraints and evaluating jump conditions with the extended finite element method. *Int J Numer Methods Eng*. 2004;61(14):2508-2535.

38. Moës N, Béchet E, Tourbier M. Imposing Dirichlet boundary conditions in the extended finite element method. *Int J Numer Methods Eng*. 2006;67(12):1641-1669.

39. Hautefeuille M, Annavarapu C, Dolbow JE. Robust imposition of Dirichlet boundary conditions on embedded surfaces. *Int J Numer Methods Eng*. 2012;90(1):40-64.

40. Khoei AR. *Extended Finite Element Method: Theory and Applications*. John Wiley & Sons; 2014.

41. Fernandez RT. *Natural Convection from Cylinders Buried in Porous Media*. PhD thesis. University of California; 1972.

42. Lujan CA. *Three-phase Flow Analysis of NAPL Spills in Partially Water-saturated Soils*. PhD thesis. Colorado State University; 1985.

43. Brooks RH, Corey AT. Properties of porous media affecting fluid flow. *J Irrig Drain Eng, ASCE*. 1966;92:61-68.

44. Reddy JN. *An Introduction to Nonlinear Finite Element Analysis*. Oxford University Press; 2004.

45. Mergheim J, Kuhl E, Steinmann P. A finite element method for the computational modeling of cohesive cracks. *Int J Numer Methods Eng*. 2005;63:276-289.

46. Lewis RW, Schrefler BA. *The Finite Element Method in the Static and Dynamic Deformation and Consolidation of Porous Media*. Wiley; 1998.

47. Moës N, Cloirec M, Cartraud P, Remacle JF. A computational approach to handle complex microstructure geometries. *Comput Methods Appl Mech Eng*. 2003;192:3163-3177.

48. Hirmand M, Vahab M, Khoei AR. An augmented Lagrangian contact formulation for frictional discontinuities with the extended finite element method. *Finite Elements Anal Design*. 2015;107:28-43.

49. Liu F, Borja RI. A contact algorithm for frictional crack propagation with the extended finite element method. *Int J Numer Methods Eng*. 2008;76(10):1489-1512.

APPENDIX A

$$\frac{1}{Q_{ww}} = \left(\frac{n'S_w}{K_w} - n'\left(\frac{\partial S_w}{\partial p_{cgw}} + \frac{\partial S_w}{\partial p_{cnw}} \right) \right.$$

$$+ S_w \frac{\alpha - n'}{K_s} \left(S_w - \left(\frac{\partial S_w}{\partial p_{cnw}} + \frac{\partial S_w}{\partial p_{cgw}} \right)(p_w - p_g) - \left(\frac{\partial S_n}{\partial p_{cnw}} + \frac{\partial S_n}{\partial p_{cgw}} \right)(p_n - p_g) \right) \right),$$

$$\frac{1}{Q_{wg}} = \left(n'\left(\frac{\partial S_w}{\partial p_{cgw}} \right) \right.$$

$$+ S_w \frac{\alpha - n'}{K_s} \left((1 - S_w - S_n) + \left(\frac{\partial S_w}{\partial p_{cgw}} \right)(p_w - p_g) + \left(\frac{\partial S_n}{\partial p_{cgw}} \right)(p_n - p_g) \right) \right),$$

$$\frac{1}{Q_{wn}} = \left(n'\left(\frac{\partial S_w}{\partial p_{cnw}} \right) \right.$$

$$+ S_w \frac{\alpha - n'}{K_s} \left((S_n) + \left(\frac{\partial S_w}{\partial p_{cnw}} \right)(p_w - p_g) + \left(\frac{\partial S_n}{\partial p_{cnw}} \right)(p_n - p_g) \right) \right),$$

$$\beta_{wT} = -\left(n'S_w\beta_w + S_w(\alpha - n')\beta_s \right) \tag{A1}$$

$$\frac{1}{Q_{gw}} = \left(n'\left(\frac{\partial S_w}{\partial p_{cgw}} + \frac{\partial S_n}{\partial p_{cgw}} + \frac{\partial S_w}{\partial p_{cnw}} + \frac{\partial S_n}{\partial p_{cnw}} \right) \right.$$

$$+ \frac{\alpha - n'}{K_s}(1 - S_w - S_n)\left(S_w - \left(\frac{\partial S_w}{\partial p_{cnw}} + \frac{\partial S_w}{\partial p_{cgw}} \right)(p_w - p_g) - \left(\frac{\partial S_n}{\partial p_{cnw}} + \frac{\partial S_n}{\partial p_{cgw}} \right)(p_n - p_g) \right) \right),$$

$$\frac{1}{Q_{gg}} = \left(n'\frac{(1 - S_w - S_n)}{K_g} - n'\left(\frac{\partial S_w}{\partial p_{cgw}} + \frac{\partial S_n}{\partial p_{cgw}} \right) \right.$$

$$+ \frac{\alpha - n'}{K_s}(1 - S_w - S_n)\left((1 - S_w - S_n) + \left(\frac{\partial S_w}{\partial p_{cgw}} \right)(p_w - p_g) + \left(\frac{\partial S_n}{\partial p_{cgw}} \right)(p_n - p_g) \right) \right),$$

$$\frac{1}{Q_{gn}} = \left(-n'\left(\frac{\partial S_w}{\partial p_{cnw}} + \frac{\partial S_n}{\partial p_{cnw}} \right) \right.$$

$$+ \frac{\alpha - n'}{K_s}(1 - S_w - S_n)\left(S_n + \left(\frac{\partial S_w}{\partial p_{cnw}} \right)(p_w - p_g) + \left(\frac{\partial S_n}{\partial p_{cnw}} \right)(p_n - p_g) \right) \right),$$

$$\beta_{gT} = -\left(n'(1 - S_w - S_n)\beta_g + (\alpha - n')(1 - S_w - S_n)\beta_s \right) \tag{A2}$$

$$\frac{1}{Q_{nw}} = \left(-n'\left(\frac{\partial S_n}{\partial p_{cgw}} + \frac{\partial S_n}{\partial p_{cnw}} \right) \right.$$

$$+ \frac{\alpha - n'}{K_s}(S_n)\left(S_w - \left(\frac{\partial S_w}{\partial p_{cnw}} + \frac{\partial S_w}{\partial p_{cgw}} \right)(p_w - p_g) - \left(\frac{\partial S_n}{\partial p_{cnw}} + \frac{\partial S_n}{\partial p_{cgw}} \right)(p_n - p_g) \right) \right),$$

$$\frac{1}{Q_{ng}} = \left(n'\left(\frac{\partial S_n}{\partial p_{cgw}} \right) \right.$$

$$+ \frac{\alpha - n'}{K_s}(S_n)\left((1 - S_w - S_n) + \left(\frac{\partial S_w}{\partial p_{cgw}} \right)(p_w - p_g) + \left(\frac{\partial S_n}{\partial p_{cgw}} \right)(p_n - p_g) \right) \right),$$

$$\frac{1}{Q_{nn}} = \left((n'\frac{S_n}{K_n}) + n'\left(\frac{\partial S_n}{\partial p_{cnw}} \right) \right.$$

$$+ \frac{\alpha - n'}{K_s}(S_n)\left(S_n + \left(\frac{\partial S_w}{\partial p_{cnw}} \right)(p_w - p_g) + \left(\frac{\partial S_n}{\partial p_{cnw}} \right)(p_n - p_g) \right) \right),$$

$$\beta_{nT} = -\left(n'(S_n)\beta_n + (\alpha - n')(S_n)\beta_s \right) \tag{A3}$$

APPENDIX B

$$[M^e]^{11}_{IJ} = \int_{A_e} \rho_{av}(\boldsymbol{\psi}^1_I)^\top \boldsymbol{\psi}^1_J d\Omega, \quad [M^e]^{22}_{IJ} = \int_{A_e} \rho_{av}(\boldsymbol{\psi}^2_I)^\top \boldsymbol{\psi}^2_J d\Omega \tag{B1}$$

$$[M^e]^{31}_{IJ} = \int_{A_e} (\rho_w k_{w_x})(\boldsymbol{\psi}^3_I)^\top_{,x} \boldsymbol{\psi}^1_J d\Omega,$$

$$[M^e]^{32}_{IJ} = \int_{A_e} (\rho_w k_{w_y})(\boldsymbol{\psi}^3_I)^\top_{,y} \boldsymbol{\psi}^2_J d\Omega \tag{B2}$$

$$[M^e]^{41}_{IJ} = \int_{A_e} (\rho_g k_{g_x})(\boldsymbol{\psi}^4_I)^\top_{,x} \boldsymbol{\psi}^1_J d\Omega, \quad [M^e]^{42}_{IJ} = \int_{A_e} (\rho_g k_{g_y})(\boldsymbol{\psi}^4_I)^\top_{,y} \boldsymbol{\psi}^2_J d\Omega \tag{B3}$$

$$[M^e]^{51}_{IJ} = \int_{A_e} (\rho_n k_{n_x})(\boldsymbol{\psi}^5_I)^\top_{,x} \boldsymbol{\psi}^1_J d\Omega, \quad [M^e]^{52}_{IJ} = \int_{A_e} (\rho_n k_{n_y})(\boldsymbol{\psi}^5_I)^\top_{,y} \boldsymbol{\psi}^2_J d\Omega \tag{B4}$$

$$[K^e]^{11}_{IJ} = \int_{A_e} \left(C_{11}(\boldsymbol{\psi}^1_I)^\top_{,x}(\boldsymbol{\psi}^1_J)_{,x} + C_{13}(\boldsymbol{\psi}^1_I)^\top_{,x}(\boldsymbol{\psi}^1_J)_{,y} + C_{31}(\boldsymbol{\psi}^1_I)^\top_{,y}(\boldsymbol{\psi}^1_J)_{,x} + C_{33}(\boldsymbol{\psi}^1_I)^\top_{,y}(\boldsymbol{\psi}^1_J)_{,y}\right) d\Omega \tag{B5}$$

$$[K^e]^{12}_{IJ} = \int_{A_e} \left(C_{12}(\boldsymbol{\psi}^1_I)^\top_{,x}(\boldsymbol{\psi}^2_J)_{,y} + C_{13}(\boldsymbol{\psi}^1_I)^\top_{,x}(\boldsymbol{\psi}^2_J)_{,x} + C_{32}(\boldsymbol{\psi}^1_I)^\top_{,y}(\boldsymbol{\psi}^2_J)_{,y} + C_{33}(\boldsymbol{\psi}^1_I)^\top_{,y}(\boldsymbol{\psi}^2_J)_{,x}\right) d\Omega \tag{B6}$$

$$[K^e]^{13}_{IJ} = \int_{A_e} -\alpha(S_w)(\boldsymbol{\psi}^1_I)^\top_{,x}(\boldsymbol{\psi}^3_J) d\Omega \tag{B7}$$

$$[K^e]^{14}_{IJ} = \int_{A_e} -\alpha(1 - S_w - S_n)(\boldsymbol{\psi}^1_I)^\top_{,x}(\boldsymbol{\psi}^4_J) d\Omega \tag{B8}$$

$$[K^e]^{15}_{IJ} = \int_{A_e} -\alpha(S_n)(\boldsymbol{\psi}^1_I)^\top_{,x}(\boldsymbol{\psi}^5_J) d\Omega \tag{B9}$$

$$[K^e]^{16}_{IJ} = \int_{A_e} \left(-(C_{11}\alpha_{11} + C_{12}\alpha_{22})(\boldsymbol{\psi}^1_I)^\top_{,x}(\boldsymbol{\psi}^6_J) - (C_{31}\alpha_{11} + C_{32}\alpha_{22})(\boldsymbol{\psi}^1_I)^\top_{,y}(\boldsymbol{\psi}^6_J)\right) d\Omega \tag{B10}$$

$$[K^e]^{21}_{IJ} = \int_{A_e} \left(C_{21}(\boldsymbol{\psi}^2_I)^\top_{,y}(\boldsymbol{\psi}^1_J)_{,x} + C_{23}(\boldsymbol{\psi}^2_I)^\top_{,y}(\boldsymbol{\psi}^1_J)_{,y} + C_{31}(\boldsymbol{\psi}^2_I)^\top_{,x}(\boldsymbol{\psi}^1_J)_{,x} + C_{33}(\boldsymbol{\psi}^2_I)^\top_{,x}(\boldsymbol{\psi}^1_J)_{,y}\right) d\Omega \tag{B11}$$

$$[K^e]^{22}_{IJ} = \int_{A_e} \left(C_{22}(\boldsymbol{\psi}^2_I)^\top_{,y}(\boldsymbol{\psi}^2_J)_{,y} + C_{23}(\boldsymbol{\psi}^2_I)^\top_{,y}(\boldsymbol{\psi}^2_J)_{,x} + C_{32}(\boldsymbol{\psi}^2_I)^\top_{,x}(\boldsymbol{\psi}^2_J)_{,y} + C_{33}(\boldsymbol{\psi}^2_I)^\top_{,x}(\boldsymbol{\psi}^2_J)_{,x}\right) d\Omega \tag{B12}$$

$$[K^e]^{23}_{IJ} = \int_{A_e} -\alpha(S_w)(\boldsymbol{\psi}^2_I)^\top_{,y}(\boldsymbol{\psi}^3_J) d\Omega \tag{B13}$$

$$[K^e]^{24}_{IJ} = \int_{A_e} -\alpha(1 - S_w - S_n)(\boldsymbol{\psi}^2_I)^\top_{,y}(\boldsymbol{\psi}^4_J) d\Omega \tag{B14}$$

$$[K^e]^{25}_{IJ} = \int_{A_e} -\alpha(S_n)(\boldsymbol{\psi}^2_I)^\top_{,y}(\boldsymbol{\psi}^5_J) d\Omega \tag{B15}$$

$$[K^e]^{26}_{IJ} = \int_{A_e} \left(-(C_{21}\alpha_{11} + C_{22}\alpha_{22})(\boldsymbol{\psi}^2_I)^\top_{,y}(\boldsymbol{\psi}^6_J) - (C_{31}\alpha_{11} + C_{32}\alpha_{22})(\boldsymbol{\psi}^2_I)^\top_{,x}(\boldsymbol{\psi}^6_J)\right) d\Omega \tag{B16}$$

$$[K^e]^{33}_{IJ} = \int_{A_e} \left(k_{w_x}(\boldsymbol{\psi}^3_I)^\top_{,x}(\boldsymbol{\psi}^3_J)_{,x} + k_{w_y}(\boldsymbol{\psi}^3_I)^\top_{,y}(\boldsymbol{\psi}^3_J)_{,y}\right) d\Omega \tag{B17}$$

$$[K^e]^{44}_{IJ} = \int_{A_e} \left(k_{g_x}(\boldsymbol{\psi}^4_I)^\top_{,x}(\boldsymbol{\psi}^4_J)_{,x} + k_{g_y}(\boldsymbol{\psi}^4_I)^\top_{,y}(\boldsymbol{\psi}^4_J)_{,y}\right) d\Omega \tag{B18}$$

$$[K^e]^{55}_{IJ} = \int_{A_e} \left(k_{n_x}(\boldsymbol{\psi}^5_I)^\top_{,x}(\boldsymbol{\psi}^5_J)_{,x} + k_{n_y}(\boldsymbol{\psi}^5_I)^\top_{,y}(\boldsymbol{\psi}^5_J)_{,y}\right) d\Omega \tag{B19}$$

$$[K^e]_{IJ}^{66} = \int_{A_e} \left(\rho_w C_w k_{w_x}(-p_{w,x}) + \rho_g C_g k_{g_x}(-p_{g,x}) + \rho_n C_n k_{n_x}(-p_{n,x}) \right) \left((\boldsymbol{\psi}_I^6)^\top (\boldsymbol{\psi}_J^6)_{,x} \right) d\Omega$$

$$+ \int_{A_e} \left(\rho_w C_w k_{w_y}(-p_{w,y}) + \rho_g C_g k_{g_y}(-p_{g,y}) + \rho_n C_n k_{n_y}(-p_{n,y}) \right) \left((\boldsymbol{\psi}_I^6)^\top (\boldsymbol{\psi}_J^6)_{,y} \right) d\Omega$$

$$+ \int_{A_e} \left((\rho_w^2 C_w k_{w_x} + \rho_g^2 C_g k_{g_x} + \rho_n^2 C_n k_{n_x})(b_x) \right) \left((\boldsymbol{\psi}_I^6)^\top (\boldsymbol{\psi}_J^6)_{,x} \right) d\Omega$$

$$+ \int_{A_e} \left((\rho_w^2 C_w k_{w_y} + \rho_g^2 C_g k_{g_y} + \rho_n^2 C_n k_{n_y})(b_y) \right) \left((\boldsymbol{\psi}_I^6)^\top (\boldsymbol{\psi}_J^6)_{,y} \right) d\Omega$$

$$- \int_{A_e} \left((\rho_w^2 C_w k_{w_x} + \rho_g^2 C_g k_{g_x} + \rho_n^2 C_n k_{n_x})(\ddot{u}_x) \right) \left((\boldsymbol{\psi}_I^6)^\top (\boldsymbol{\psi}_J^6)_{,x} \right) d\Omega$$

$$- \int_{A_e} \left((\rho_w^2 C_w k_{w_y} + \rho_g^2 C_g k_{g_y} + \rho_n^2 C_n k_{n_y})(\ddot{u}_y) \right) \left((\boldsymbol{\psi}_I^6)^\top (\boldsymbol{\psi}_J^6)_{,y} \right) d\Omega$$

$$+ \int_{A_e} \left(\kappa_{av_x}(\boldsymbol{\psi}_I^6)_{,x}^\top (\boldsymbol{\psi}_J^6)_{,x} + \kappa_{av_y}(\boldsymbol{\psi}_I^6)_{,y}^\top (\boldsymbol{\psi}_J^6)_{,y} \right) \tag{B20}$$

$$[C^e]_{IJ}^{31} = \int_{A_e} E_{sw}\,\alpha(\boldsymbol{\psi}_I^3)^\top (\boldsymbol{\psi}_J^1)_{,x} d\Omega \tag{B21}$$

$$[C^e]_{IJ}^{32} = \int_{A_e} E_{sw}\,\alpha(\boldsymbol{\psi}_I^3)^\top (\boldsymbol{\psi}_J^2)_{,y} d\Omega \tag{B22}$$

$$[C^e]_{IJ}^{33} = \int_{A_e} \frac{1}{Q_{ww}}(\boldsymbol{\psi}_I^3)^\top (\boldsymbol{\psi}_J^3) d\Omega \tag{B23}$$

$$[C^e]_{IJ}^{34} = \int_{A_e} \frac{1}{Q_{wg}}(\boldsymbol{\psi}_I^3)^\top (\boldsymbol{\psi}_J^4) d\Omega \tag{B24}$$

$$[C^e]_{IJ}^{35} = \int_{A_e} \frac{1}{Q_{wn}}(\boldsymbol{\psi}_I^3)^\top (\boldsymbol{\psi}_J^5) d\Omega \tag{B25}$$

$$[C^e]_{IJ}^{36} = \int_{A_e} \beta_{wT}(\boldsymbol{\psi}_I^3)^\top (\boldsymbol{\psi}_J^6) d\Omega \tag{B26}$$

$$[C^e]_{IJ}^{41} = \int_{A_e} (1 - S_w - S_n)\alpha(\boldsymbol{\psi}_I^4)^\top (\boldsymbol{\psi}_J^1)_{,x} d\Omega \tag{B27}$$

$$[C^e]_{IJ}^{42} = \int_{A_e} (1 - S_w - S_n)\alpha(\boldsymbol{\psi}_I^4)^\top (\boldsymbol{\psi}_J^2)_{,y} d\Omega \tag{B28}$$

$$[C^e]_{IJ}^{43} = \int_{A_e} \frac{1}{Q_{gw}}(\boldsymbol{\psi}_I^4)^\top (\boldsymbol{\psi}_J^3) d\Omega \tag{B29}$$

$$[C^e]_{IJ}^{44} = \int_{A_e} \frac{1}{Q_{gg}}(\boldsymbol{\psi}_I^4)^\top (\boldsymbol{\psi}_J^4) d\Omega \tag{B30}$$

$$[C^e]_{IJ}^{45} = \int_{A_e} \frac{1}{Q_{gn}}(\boldsymbol{\psi}_I^4)^\top (\boldsymbol{\psi}_J^5) d\Omega \tag{B31}$$

$$[C^e]_{IJ}^{46} = \int_{A_e} \beta_{gT}(\boldsymbol{\psi}_I^4)^\top (\boldsymbol{\psi}_J^6) d\Omega \tag{B32}$$

$$[C^e]_{IJ}^{51} = \int_{A_e} (S_n)\alpha(\boldsymbol{\psi}_I^5)^\top (\boldsymbol{\psi}_J^1)_{,x} d\Omega \tag{B33}$$

$$[C^e]_{IJ}^{52} = \int_{A_e} (S_n)\alpha(\boldsymbol{\psi}_I^5)^\top (\boldsymbol{\psi}_J^2)_{,y} d\Omega \tag{B34}$$

$$[C^e]_{IJ}^{53} = \int_{A_e} \frac{1}{Q_{nw}} (\boldsymbol{\psi}_I^5)^\top (\boldsymbol{\psi}_J^3) d\Omega \tag{B35}$$

$$[C^e]_{IJ}^{54} = \int_{A_e} \frac{1}{Q_{ng}} (\boldsymbol{\psi}_I^5)^\top (\boldsymbol{\psi}_J^4) d\Omega \tag{B36}$$

$$[C^e]_{IJ}^{55} = \int_{A_e} \frac{1}{Q_{nn}} (\boldsymbol{\psi}_I^5)^\top (\boldsymbol{\psi}_J^5) d\Omega \tag{B37}$$

$$[C^e]_{IJ}^{56} = \int_{A_e} \beta_{nT} (\boldsymbol{\psi}_I^5)^\top (\boldsymbol{\psi}_J^6) d\Omega \tag{B38}$$

$$[C^e]_{IJ}^{66} = \int_{A_e} \left(\rho_s (1 - n') C_s + \rho_w (n') S_w C_w + \rho_n (n') S_n C_n + \rho_g (n')(1 - S_w - S_n) C_g \right) (\boldsymbol{\psi}_I^6)^\top (\boldsymbol{\psi}_J^6) d\Omega \tag{B39}$$

$$\boldsymbol{F}_I^{e1} = \int_{A_e} \left(\rho_{av} (b_x) (\boldsymbol{\psi}_I^1)^\top \right) d\Omega - \int_{A_e} \left((C_{11}\alpha_{11} + C_{12}\alpha_{22})(T_0)(\boldsymbol{\psi}_I^1)_{,x}^\top + (C_{31}\alpha_{11} + C_{32}\alpha_{22})(T_0)(\boldsymbol{\psi}_I^1)_{,y}^\top \right) d\Omega$$
$$+ \int_{s_e^t} \left(\bar{t}_x (\boldsymbol{\psi}_I^1)^\top \right) d\Gamma_t + \int_{s_e^d} \left(\bar{t}_{d_x} (\boldsymbol{\psi}_I^1)^\top \right) d\Gamma_d \tag{B40}$$

$$+ \boldsymbol{F}_I^{e2} = \int_{A_e} \left(\rho_{av} (b_y) (\boldsymbol{\psi}_I^2)^\top \right) d\Omega - \int_{A_e} \left((C_{21}\alpha_{11} + C_{22}\alpha_{22})(T_0)(\boldsymbol{\psi}_I^2)_{,y}^\top + (C_{31}\alpha_{11} + C_{32}\alpha_{22})(T_0)(\boldsymbol{\psi}_I^2)_{,x}^\top \right) d\Omega$$
$$+ \int_{s_e^t} \left(\bar{t}_y (\boldsymbol{\psi}_I^2)^\top \right) d\Gamma_t + \int_{s_e^d} \left(\bar{t}_{d_y} (\boldsymbol{\psi}_I^2)^\top \right) d\Gamma_d \tag{B41}$$

$$\boldsymbol{F}_I^{e3} = \int_{A_e} \left((k_{w_x} \rho_w)(\boldsymbol{\psi}_I^3)_{,x}^\top b_x + (k_{w_y} \rho_w)(\boldsymbol{\psi}_I^3)_{,y}^\top b_y \right) d\Omega - \int_{s_e^{q_w}} \bar{q}_w (\boldsymbol{\psi}_I^3)^\top d\Gamma \tag{B42}$$

$$\boldsymbol{F}_I^{e4} = \int_{A_e} \left((k_{g_x} \rho_g)(\boldsymbol{\psi}_I^4)_{,x}^\top b_x + (k_{g_y} \rho_g)(\boldsymbol{\psi}_I^4)_{,y}^\top b_y \right) d\Omega - \int_{s_e^{q_g}} \bar{q}_g (\boldsymbol{\psi}_I^4)^\top d\Gamma \tag{B43}$$

$$\boldsymbol{F}_I^{e5} = \int_{A_e} \left((k_{n_x} \rho_n)(\boldsymbol{\psi}_I^5)_{,x}^\top b_x + (k_{n_y} \rho_n)(\boldsymbol{\psi}_I^5)_{,y}^\top b_y \right) d\Omega - \int_{s_e^{q_n}} \bar{q}_n (\boldsymbol{\psi}_I^5)^\top d\Gamma \tag{B44}$$

$$\boldsymbol{F}_I^{e6} = - \int_{s_e^{q_T}} \bar{q}_T (\boldsymbol{\psi}_I^6)^\top d\Gamma \tag{B45}$$

in which e is either 1 or 2 for the superimposed elements one and two, respectively, and s_e^t, s_e^d are the portions of superimposed element e on the traction boundary Γ_t and discontinuity surface Γ_d, respectively. $s_e^{q_w}$, $s_e^{q_g}$, $s_e^{q_n}$ are the portions of superimposed element e on the fluid flux boundary of water phase Γ_{q_w}, gas phase Γ_{q_g} and non-aqueous phase Γ_{q_n}, respectively, and $s_e^{q_T}$ indicates the portions of superimposed element e on the thermal flux boundary Γ_{q_T}. $C_{\gamma\beta}$ ($\gamma, \beta = 1$ through 3) are the components of the elastic stiffness tensor $\boldsymbol{C}$ and $\alpha_{\gamma\gamma}$ ($\gamma = 1$ through 2) are the components of the thermal expansion tensor $\boldsymbol{\alpha}$. It is important to mention that in isotropic thermal expansion behaviour, $\alpha_{11} = \alpha_{22} = \beta_s/3$. k_{a_x} and k_{a_y} ($a = w, g, n$) are the components of the permeability tensor of the porous medium to the pore fluid a in x and y (i.e. horizontal and vertical) directions, respectively. Symbols $(,x)$ and $(,y)$ indicate partial derivative with respect to x and y, respectively.